Derived Observations from Frequently-Sampled Microwave Measurements of Precipitation and their Relations to Atmospheric Dynamics and Thermodynamics

Sy O.O. ◇[1], Haddad Z.S. ◇[2], Stephens G.L. ◇, Hristova-Veleva S. ◇

◇ *Jet Propulsion Laboratory, California Institute of Technology, Pasadena, California,*

[1] Ousmane.O.Sy@jpl.nasa.gov, [2] Ziad.S.Haddad@jpl.nasa.gov

5 December 2015
submitted to IEEE Trans. Geosci. Rem. Sens.

Contents

Abstract

This article discusses the high added-value of using frequent tri-dimensional radar observations of the atmosphere to capture the dynamics of rapidly evolving weather systems. The novelty of our approach resides in its application to spaceborne radars, since none of the existing spaceborne radars is capable of such frequent observations (within minutes). Nonetheless, recent advances in small-satellite and radar technologies, such as the Radar in Cubesat (RainCube) developed at the Jet Propulsion Laboratory, have paved the way for the design of a convoy of spaceborne radars to perform the targeted measurements.

The joint use of the radar reflectivities Z and their time derivatives $d_t Z$ provides rich and unique information about the dynamics of the atmosphere. As illustrated using NEXRAD measurements of a blizzard coupled with an atmospheric river in California and of tropical storms making landfall in Florida and Hawaii, maps of $d_t Z$ reveal *latent horizontal features* about locations of sources and sinks of moisture. The robust relation between $d_t Z$ and the rate of change of the condensed-water mass M is also confirmed using numerical-weather simulations of the topical cyclone Isabel with a radiative-transfer code to simulate Ka-band measurements of Z from space. The high resolution of these simulations in space and time allows also to demonstrate that *vertical dynamic variables* such as fluxes of dry and moist air in convection can be retrieved accurately from Z and $d_t Z$ using a Bayesian algorithm.

Lastly, we discuss some of the constraints involved in the design of a convoy of two satellites, each embarking a mini nadir-pointing Ka-band Atmospheric Radar (miniKaAR). Our simulations show that, with a convoy of two spacecraft separated by ~ 90 s, each with a pointing accuracy of $\sim 0.025^\circ$ in rms error, a sensitivity of 17 dBZ and a precision of 1 dBZ, the proposed mission will observe more than 70% of the tropical convection between 5 and 10 km of altitude and resolve the time variations of fluxes of convective air masses.

1 Introduction

Spaceborne profiling radars provide valuable tri-dimensional measurements of clouds and precipitation for which in-situ data are often challenging to obtain. From these global observations, researchers and operational forecasters are able to estimate meteorological quantities such the mass of condensed water or the precipitation rate from the measured reflectivity factor Z, the mean characteristic size (e.g. mass-weighted mean diameter) of hydrometeors from dual-wavelength ratios, or latent-heating profiles from the reflectivity and mean Doppler velocity [1, 5, 7, 9].

While the current fleet of spaceborne precipitation radars provides a good spatial coverage of the atmosphere of the Earth, it does not allow to properly capture the time variation of cloud or precipitation systems that have life cycles in the order of 30 minutes to a few hours [13]. While a radar on a geostationary platform would fulfill the requirement of frequent temporal sampling, such an instrument does not exist yet partly due to the difficulty of achieving a high spatial

resolution from a geostationary orbit with an antenna of reasonable size. The existing low-Earth orbiting satellites that carry radars such as CloudSat (16 days revisit time), the Tropical Rainfall Measurement Mission (TRMM, 11–12 hours repeat time) or the core satellite of the Global Precipitation Mission (GPM, 3 hour repeat time) are such that between two consecutive passes of the instrument over a given region the cloud or storm of interest will have changed significantly if not disappeared.

The use of frequent high-resolution observations of the atmosphere over a given region allows to assess the dynamic evolution of the atmospheric state parameters by computing their derivatives. These derivatives help quantify processes such as mass or heat fluxes, which are essential parameters of storms and tropical cyclones [7]. Hence, the computed derivatives would be particularly relevant for their assimilation in numerical weather forecasting models [14].

The objective of this article is to illustrate the usefulness of derivatives of frequent high-resolution radar reflectivity observations to characterize the atmosphere. The added value of the computed derivatives will be shown by i) illustrating how the spatial patterns of these derivatives differ from those of the initial radar reflectivity, ii) demonstrating the robustness of the correlation between derivatives of the radar reflectivities and derivatives of the condensed water mass, and iii) showing how these variables help estimate dynamic atmospheric parameters such as vertical fluxes of dry or moist air.

To the best of the authors' knowledge, such a use of radar observations is uncommon. Among the rare applications is the work done in morphing where sequences of measurements are used to rebuild the time evolution of the radar singal. This amounts to interpolating the measurements in a spatially and physically meaningful way at a spatial and temporal resolution finer than the one of the measured data [18, 24]. In our case, the objective is not to interpolate the data at a finer resolution than available, but rather to exploit the information carried by the derivatives of the radar data.

To this end, the article is structured around three parts. First, the added value of high-resolution radar data sets is shown using ground-based measurements of reflectivity factors Z acquired by the network of S-band ($\sim$ 3 GHz) NEXRAD radars. Due to the "coarse" sampling rate of NEXRAD ($\sim$4 to 6 min in precipitation mode), the time derivatives $d_t Z$ computed by finite differences account for the advection, which is estimated robustly using a digital-image correlation technique [3]. Three extreme-weather NEXRAD data sets are considered, viz. i) the Northern California super-storm of January 2008, which was coupled with an atmospheric river, ii) the tropical cyclone Fay as it made landfall in Florida in August 2008, and iii) the tropical storm Iselle, which made landfall on Big Island, Hawaii, in August 2014. These three examples reveal patterns in the horizontal distributions of $d_t Z$, which differ from those of the radar reflectivities themselves and therefore call for a quantitative analysis of the derived products in terms of atmospheric variables particularly along the vertical dimension.
This is done in the second part of the article, where high-resolution cloud-resolving-model simulations of a cyclogenesis are used. These Weather Research and Forecasting (WRF) simulations

are fed to a radiative-transfer code to obtain Ka-band ($\sim$ 35 GHz) radar reflectivity data observed by a spaceborne radar with a horizontal resolution similar to GPM's Ka-band radar and a very fine vertical resolution (the native WRF vertical resolution). Three different micro-physical schemes are employed during these radiative transfer simulations, viz. Lin, WSM6 and an empirical scheme devised by the authors. The analysis of these refined data allows to relate the derivatives $d_t Z$ of the synthetic radar signatures to the rate of change of condensed-water mass $d_t M$, in a significantly more robust way than traditional single-frequency $Z - M$ relationships. Moreover, the fine vertical sampling of the simulated Z and $d_t Z$ allows to retrieve vertical dynamic variables such as transports of air masses in convective cores. The Bayesian-retrieval algorithm that we propose yields accurate estimates of both dry and moist air mass fluxes in the upper troposphere, which in turns informs on detrainment processes at those altitudes.
In light of these results, the third and last part of the article discussed some design criteria for the acquisition of frequent radar measurements using a convoy a low-Earth orbiting (LEO) CubeSats. In the propsed mission, each spacecraft would carry a mini nadir-pointing Ka-band Atmospheric Radar (MiniKaAR), which uses the Radar in CubeSat (RainCube) technology recently developed at JPL. A preliminary performance analysis of such a train of radars provides guidelines about the optimal inter-satellite separation, and the sensitivity of the radar measurements and retrievals to pointing uncertainties.

The outline of this article is as follows. First, a preliminary heuristic analysis is presented in Section 2 to discuss the relationship between derivatives of radar reflectivities and derivatives of the mass of condensed water. Section 3.1 then illustrates the spatial patterns of these derivatives using NEXRAD measurements of three extreme-weather events, viz. a blizzard in Northern California, a tropical cyclone making landfall and tropical storm interacting with complex orography. This part involves uniquely measurements and no numerical model simulation of the atmosphere. Next, in Section 4, numerical simulations of the atmosphere are used with radiative-transfer simulations to quantify the relation between derivatives of the radar reflectivities and atmospheric thermodynamic variables. In Section 5, we analyze the design criteria that are required to obtain frequent radar measurements from a train of spaceborne radars on small satellites. Conclusions are provided in Section 6.

2 Time derivatives of the radar reflectivity factors

We consider a set of reflectivity factor measurements $\{Z_{[\mathrm{mm}^6\cdot\mathrm{m}^{-3}]}(\boldsymbol{r},t),\ \boldsymbol{r}\in\Omega,\ t\in\mathcal{T}\}$ obtained from ground-based, airborne or spaceborne radars over an observation volume $\Omega\subset\mathbb{R}^3$ at times $\mathcal{T}=\{t_k\}_k\subset\mathbb{R}$. The total derivative of $Z_{[\mathrm{dBZ}]}=10\log_{10}(Z_{[\mathrm{mm}^6\cdot\mathrm{m}^{-3}]})$ then reads

$$d_t Z_{[\mathrm{dBZ}]}(\boldsymbol{r},t)=\frac{10}{\ln(10)}\frac{d_t Z_{[\mathrm{mm}^6\cdot\mathrm{m}^{-3}]}}{Z_{[\mathrm{mm}^6\cdot\mathrm{m}^{-3}]}}=\partial_t Z_{[\mathrm{dBZ}]}(\boldsymbol{r},t)+\boldsymbol{U}(\boldsymbol{r},t)\cdot\nabla_{\boldsymbol{r}} Z_{[\mathrm{dBZ}]}(\boldsymbol{r},t). \tag{1}$$

Through the presence of the advection $\boldsymbol{U}$ in Eq. (1), $d_t Z_{[\mathrm{dBZ}]}$ tracks the motion of an air parcel between radar acquisitions and measures the variation of its reflectivity factor thereby quantifying the net effect of sources and sinks of reflectivity.

Numerically, the derivative between data at instants $t_{\ell-1}$ and t_ℓ is approximated by finite differences as follows

$$d_t Z_{[\mathrm{dBZ}]}(\boldsymbol{r}, t_\ell) \approx \frac{Z_{[\mathrm{dBZ}]}(\boldsymbol{r}, t_\ell) - Z_{[\mathrm{dBZ}]}\left[\boldsymbol{r} + \boldsymbol{U}(\boldsymbol{r}, t_{\ell-1}), t_{\ell-1}\right]}{t_\ell - t_{\ell-1}}. \tag{2}$$

Typical cases where the contribution of the advection in Eq. (1) can be neglected are when the characteristic length $\boldsymbol{U}(\boldsymbol{r}, t_{\ell-1})(t_\ell - t_{\ell-1})$ is smaller than or comparable to the spatial resolution of the volume Ω, as is the case with high-resolution convective data sets that involve processes that develop essentially along the vertical.

The relevance of $d_t Z$ can be motivated in terms of the micro-physical properties of the volume observed by the radar. Indeed, it is common to relate the radar reflectivity to the total mass of condensed water M contained in the resolution volume of the radar through an empirical relationship such as [5, 9]

$$Z_{[\mathrm{mm^6 \cdot m^{-3}}]}(\boldsymbol{r}, t) \;=\; \alpha(\boldsymbol{r}, t)[M(\boldsymbol{r}, t)]^{\beta(\boldsymbol{r}, t)}, \tag{3}$$

where $\alpha(\boldsymbol{r}, t) > 0$ and $\beta(\boldsymbol{r}, t) > 0$, or in logarithmic scale,

$$Z_{[\mathrm{dBZ}]}(\boldsymbol{r}, t) = \alpha_{\mathrm{dB}}(\boldsymbol{r}, t) + 10\ \beta(\boldsymbol{r}, t) \log_{10}[M(\boldsymbol{r}, t)], \tag{4}$$

with $\alpha_{\mathrm{dB}} = 10\ \log_{10}(\alpha)$. Compared to $M(\boldsymbol{r}, t)$, which depends on and varies rapidly with the PSD and microphysical properties of the medium, the coefficients $\alpha(\boldsymbol{r}, t)$ and $\beta(\boldsymbol{r}, t)$ exhibit much slower temporal and spatial variations [8]. Hence, $d_t Z_{[\mathrm{dBZ}]}$ can be related to $d_t M$ as follows

$$d_t Z_{[\mathrm{dBZ}]}(\boldsymbol{r}, t) \;\approx\; \frac{10\beta(\boldsymbol{r}, t)}{\ln(10)} \frac{d_t M(\boldsymbol{r}, t)}{M(\boldsymbol{r}, t)}, \tag{5}$$

As a corollary to the slow variation of β with space and time, Eq. (5) shows that the linear correlation between $d_t Z_{[\mathrm{dBZ}]}$ and $d_t M/M$ should be very robust. Moreover, since β and q are positive, the sign of $d_t Z_{[\mathrm{dBZ}]}$ provides information about the dominance of either evaporation or condensation in the atmospheric volume. Such information, which is derived exclusively from the radar measurements, can be used to nudge numerical weather forecasting programs (NWP) or to identify regions of saturation where latent heating profiles can be retrieved [7].

3 Applications to NEXRAD extreme-weather measurements

Due to the absence of collocated spaceborne or airborne radar data sets with sufficiently high spatial and temporal resolutions, we resort to ground-based measurements. The network of

NEXRAD radars provides an large variety of 3D measurements for a broad range of weather conditions at numerous locations across the US. These S band radars are mainly sensitive to heavy precipitation. We consider three such extreme-weather cases, viz. the California blizzard of January 2008, the tropical cyclone Fay in Florida (August 2008) and the tropical storm Iselle in Hawaii (August 2014).

The native data is available as 3D conical volume scans produced every 5 minutes, on average. To ease the computation of derivatives, the radar data are meshed into a Cartesian grid with a resolution $\Delta_X = \Delta_Y = 1.5\ \mathrm{km}$ horizontally and $\Delta_Z = 250\ \mathrm{m}$ vertically. Given the time sampling rate of the data (i.e. 4-6 minutes), and since the events studied involve significant horizontal displacements, the advection field $\boldsymbol{U}$ must be included in the computation of the derivatives of $Z_{[\mathrm{dBZ}]}$. Failing to do so leads to erroneous estimates of the total derivative as shown in Appendix A.1 (Fig. 18).

We estimate $\boldsymbol{U}$ entirely from the radar data using a digital-image correlation technique (DICT) [21]. As detailed in Appendix A.1, given two consecutive radar acquisitions at times t_0 and t_1, the DICT identifies the field $\boldsymbol{U}$ that maximizes the statistical correlation between the field of $Z_{[\mathrm{dBZ}]}$ at t_1 and the field of $Z_{[\mathrm{dBZ}]}$ at t_0 displaced according to $\boldsymbol{U}$. The statistical optimization is performed for every vertical layer of radar data individually thereby yielding a "2.5D" advection field. This is a compromise between a crude 2D approach that would correlate vertical averages of $Z_{[\mathrm{dBZ}]}$ at t_0 and t_1, and the full 3D approach that would incur significant additional computations. The DICT is applied by computing local correlations over a neighborhood that extends over $\pm 10\ \mathrm{km}$ in the longitudinal and meridional directions thereby resolving advection speeds up to $\sim 120\ \mathrm{km} \cdot \mathrm{h}^{-1}$.

3.1 California blizzard: Sacramento, January 2008

The superstorm that hit Northern California in early 2008 led to record low pressures for a storm in the western United States and heavy precipitation in the Sierras (snow) and the Bay area (rain). The geostationary infrared image in Fig. 1 hints that the storm consisted of a baroclinic system drawing some moisture from the "Pineapple Express" to the South-West. The data used here were recorded by the NEXRAD radar in Sacramento (KDAX) during the peak of the storm, i.e. from 01-04-2008 at 18:00 to 01-05-2008 at 01:00. In particular, from 21:38 to 00:30 a squall line swept through from the North-West to the South-East, as shown in Fig. 2 (top, left). This case is a prime example of interaction between a strong precipitation system and a complex topography organized meridionally with the ocean to the West, the Northern and Southern Coastal Range mountains, the Great Valley and the Sierra Nevada to the East. Moreover, due to its relatively short life cycle (3 hours), the evolution of the squall line could not have been captured with a sufficient temporal resolution by any of the existing LEO spaceborne radars. The spatial distribution of the vertically averaged reflectivity (denoted $E_h[Z]$), and its derivative (denoted $E_h[d_t Z]$) are shown in Fig. 2 for three acquisition periods, viz. from 22:11 to 22:16 where the squall line

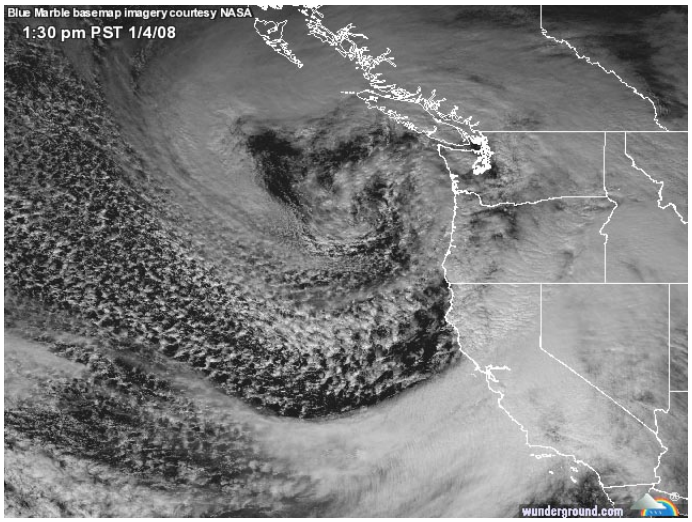

Figure 1: Visible image of the January 2008 North American Superstorm at peak intensity, on January 4, 2008. Courtesy of NASA - http://www.wunderground.com/hurricane/2007/jan04.jpg

is clearly visible (left), before the formation of the squall line (middle) and after the formation of the line (right).

A $6 \times 6\ \mathrm{km}^2$ smoothing kernel is applied to $E_h[d_t Z]$ to reduce its noisiness. The maps of $E_h[Z]$ clearly show the squall line to the East of Sacramento with a slightly slanted meridional orientation. One can note the differences in the patterns of $E_h[d_t Z]$ compared to those of $E_h[Z]$ as the regions with the largest $E_h[Z]$ do not necessarily correspond to the regions of largest $E_h[d_t Z]$, and vice versa. Furthermore, because the derivative accounts for the advection, the displacement of the squall line is not visible in the map of $E_h[d_t Z]$. The cells of increasing/decreasing reflectivity are mainly oriented from North-West to South East, i.e. parallel to the topography and orthogonal to the squall line. These patterns are confirmed by the maps of the data averaged over longer periods both before and after the formation of the squall line. On the other hand, persistent regions of increasing reflectivity can be seen in the South-West over the Bay area and in the Sierras, while a region of reflectivity sinks is present in the Great Valley. These patterns are consistent with the presence of an atmospheric river (AR) of water vapor (see figure 3), which the authors had looked for among the AR events that had been cited by the time of our analysis by Ralph et al in [19] and the references therein, in vain, but which features as one of the strongest AR events by every measure in the more complete list compiled in Ralph et al [20]. Note how the condensation appears to be triggered mostly over the coastal ranges, where the AR "makes landfall" (and compare with the center panels of figure 18), triggering a wave train propagating inland in the same direction as the AR itself.

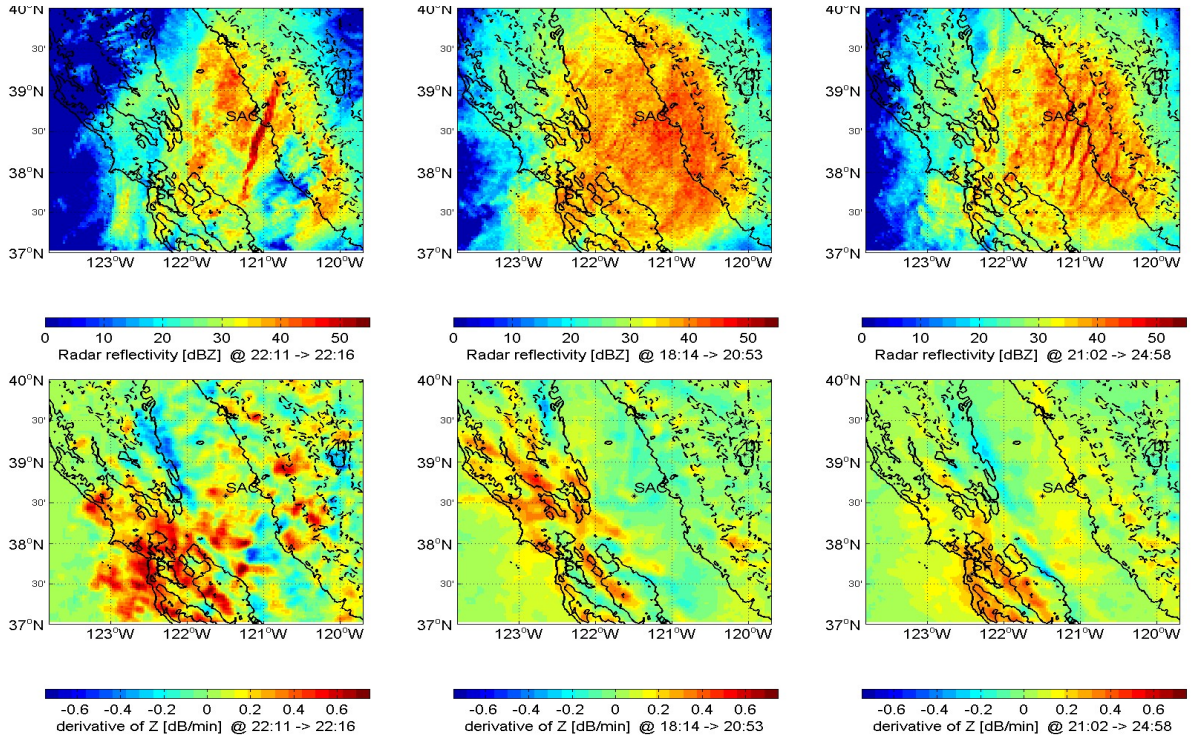

Figure 2: Maps of vertically averaged reflectivity (top) and associated derivative defined by equation (1) (bottom) as observed by the NEXRAD radar in Sacramento on 01-04-2008: temporally averaged from 22:11 to 22:16 (left) during the presence of the squall line, from 18:14 to 20:53 (middle) before the formation of the squall line, and from 21:02 to 01:00 (during squall).

3.2 Tropical storm Fay: Melbourne, Florida, August 2008

Fay was a tropical storm characterized by an erratic trajectory as it zigzagged between the ocean and land. The data analyzed here were measured by the radar in Melbourne (KMLB), Florida, from 08-19-2008 at 18:00 to 08-19-2008 at 01:00. During this time, the eye of the cyclone had a relatively slow northward motion from $(81°\mathrm{W},\ 27°\mathrm{N})$ at 18:00 up to $(80.8°\mathrm{W},\ 27.5°\mathrm{N})$ at 01:00. The maps of $E_h[Z]$ and $E_h[d_tZ]$ in Fig. 4 correspond to vertical and temporal averages over 10 minutes (left) and two hours (middle) about 22:00 and over the entire observation period (right). For the data averaged over a short duration (left column), the map of $E_h[Z]$ clearly shows the eye as well as spirals of large reflectivity associated with the rain bands. The map of $E_h[d_tZ]$ shows various regimes with concentric spirals, viz. one spiral of decaying reflectivity bracketed by an inner and outer spiral of increasing signal. Averaging over a longer duration (middle, right) confirms these features and also shows that the sources of Z (i.e. $E_h[d_tZ] > 0$) are mostly over water (East of Melbourne (KMLB)) whereas over land Z has a decreasing trend (i.e. $E_h[d_tZ] < 0$), which is consistent with the ocean acting as a source of moisture.

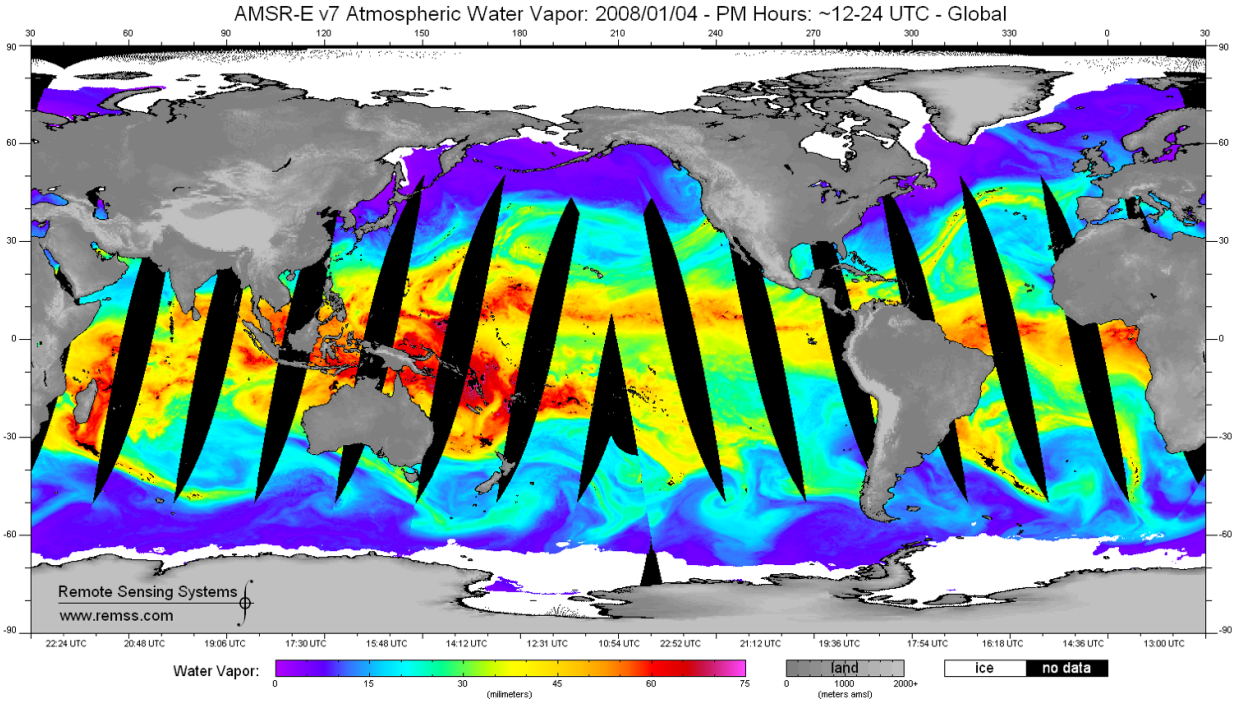

Figure 3: Water vapor derived from AMSR-E courtesy of RSS – note the atmospheric river advecting water vapor from the South West towards California.

3.3 Tropical storm Iselle: Hawaii, August 2014

The tropical cyclone Iselle was the strongest cyclone to make landfall on the Big Island of Hawaii, according to recorded history. Although by the time it reached the Big Island it was downgraded to a tropical storm, it still carried significant amounts of precipitation. The mountainous relief of the Island disrupted the spatial organization of the cyclone and eventually led to its disappearance on August 9 2014. The data analyzed here were measured by the South Shore radar (PHWA) on August 8 2014, i.e. as the cyclonic organization of Iselle (arriving from the East) was being dismantled. Indeed, one can still see the rain bands in the data averaged between 11:14 and 11:20 in Fig. 5 (left), both as larger values of $E_h[Z]$ and $E_h[d_t Z]$ along the Southern portion of the storm. For the data averaged over the early (i.e. before 16:00, middle column) and late (i.e. after 16:00, right column) observation periods, the map of $E_h[Z]$ does not seem to change significantly. However, the corresponding maps of the derivatives clearly show the differences in regimes, with significant build-up of reflectivity in the early period caused by the moisture brought by the storm, and the dissipation by precipitation that occurs in the later period as evidenced by the negative derivatives. This is yet another example of the added value of the derivatives of Z.

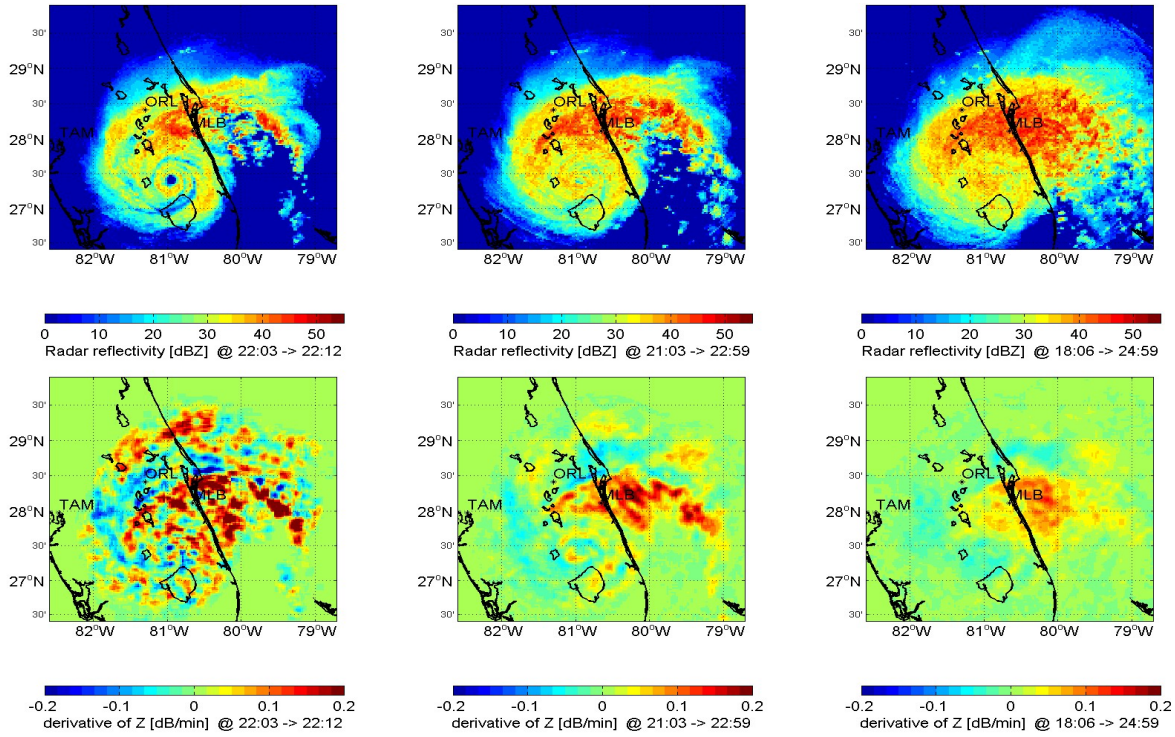

Figure 4: Maps of vertically averaged reflectivity (top) and associated derivatives (bottom) as observed by the radar in Melbourne, FL on 08-19-2008: temporally averaged between 22:00 and 22:12 (left), between 21:03 and 23:00 (middle) and between 18:06 and 01:00.

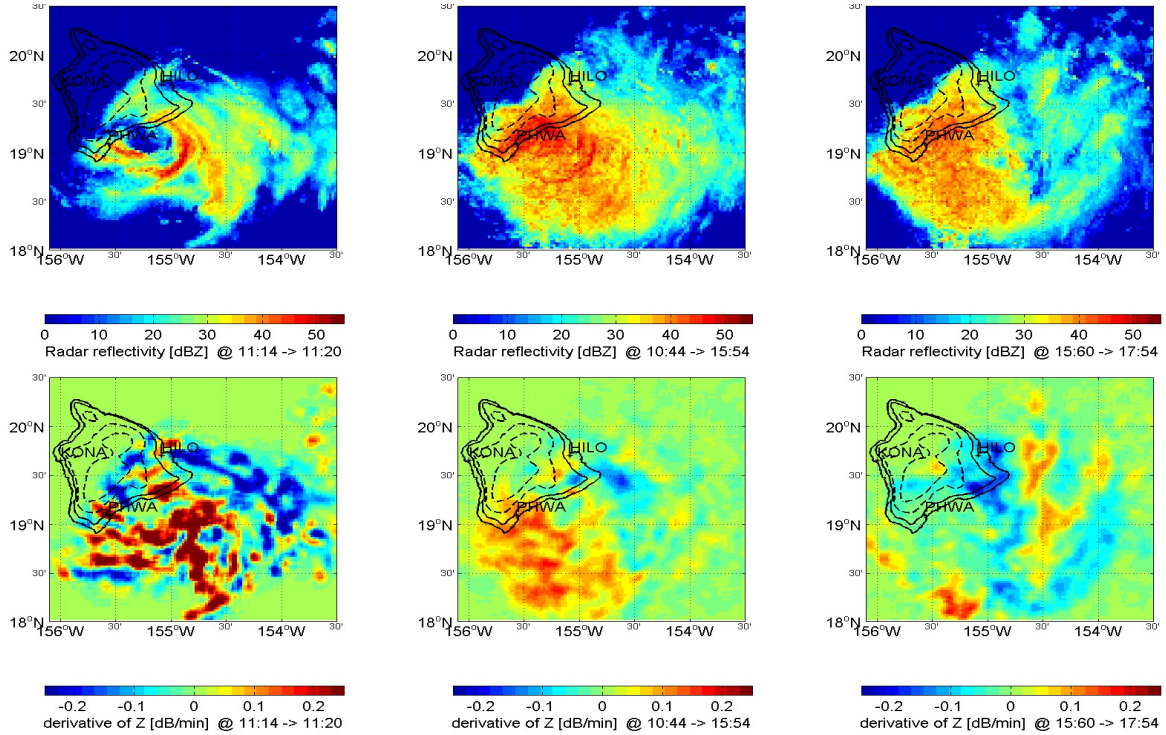

Figure 5: Maps of vertically averaged reflectivity (top) and associated derivatives (bottom) as observed by the radar at South Shore, HI on 08-08-2014: temporally averaged between 11:14 and 11:20 (left), between 10:44 and 16:00 (middle) and between 16:00 and 18:00 (right).

3.4 Comments and limitations

The cases discussed in this section illustrate how the analysis of the derivatives of the radar reflectivity provides more insight into dynamic and environmental features than the maps of Z alone (e.g. the moistening caused by the atmospheric river in the Blizzard case, moisture source from the ocean in the storm Fay, and distinction between moisture build-up and collapse by extensive precipitation of the cyclone Iselle).

The discussion has focused mainly on vertical averages of Z and $d_t Z$, and not on the vertical structure of these variables. Also, the advection, which is essential to the computation of the derivatives of the NEXRAD data, was computed via the DICT approach in 2.5D, i.e. without resolving the vertical component. Such an approach is acceptable when dealing with baroclinic systems for which horizontal gradients induce instability and the resulting motion is mostly horizontal with large-scale lifting. Even then, the vertical component of the dynamics is important, e.g. to analyze orographic enhancements or convective lifts. Moreover, for tropical convection, the instability has a critical vertical aspect whereas the lifting is horizontally localized.

While the analysis in this section has been qualitative, ultimately one needs to relate the derivatives of $Z_{[\mathrm{dBZ}]}$ to physical parameters of the atmosphere, which is non trivial. In the absence of in situ measurements as is the case here, the only alternative would be to correlate the derivatives of $Z_{[\mathrm{dBZ}]}$ measured by NEXRAD to reanalysis products. However, these reanalysis products are not available at a sufficiently fine horizontal or temporal resolution to compute meaningful derivatives consistent with the NEXRAD resolution. For instance the NASA Modern-Era Reanalysis (MERRA) products are, at best, available hourly at a horizontal resolution of 0.5° (~ 50 km), which is significantly coarser than the resolution of the NEXRAD data.

Lastly, we are also interested in finer resolutions than the NEXRAD resolutions, particularly along the vertical dimension, and in time. All these reasons motivate the use of numerical weather models for which model-truths of thermodynamic parameters of the atmosphere are available.

4 Applications to WRF simulations of Isabel

The Weather Research and Forecasting model (WRF) was used to simulate the state of the atmosphere during the incipient phase of Hurricane Isabel off the coast of Cape Verde in the Atlantic ocean ($lon \sim 30.7^\circ\mathrm{W},\ lat \sim 11.4^\circ\mathrm{N}$). A 5-nested-grids configuration was used with respective horizontal resolutions of 12 km (for the outer grid), 4 km, 1.333 km (the "d03" grid), 444 m and 148 m. Vertically, 60 pressure levels were used between the surface and 20 km, with more samples close to the surface. The WRF model was initialized with the GFS FNL analysis on 5 September 2003 at 12:00 UTC and the output was collected every 30 seconds from 06:00 to 07:00 UTC. In this article, we focus mainly on the intermediate domain (d03), which roughly spanned a domain from longitudes 36°W to 26°W and from latitudes 6°N to 16°N.

4.1 Radiative-transfer simulations

In addition to the thermodynamic variables such as the pressure, temperature and wind, the WRF includes the bulk masses of water in the forms of vapor, cloud liquid water, cloud ice, snow, graupel and snow. We use these inputs to compute the corresponding Ka-band reflectivity factors that would be observed by a spaceborne radar like GPM-Core's. The radiometric signatures of each of water species depend on fine-scale information such as the size distribution, the shape and the density of individual particles in the volume observed by the radar. All these properties are inferred through micro-physical assumptions. Different microphysical schemes are considered in order to quantify the extent to which the dependence of the instantaneous measurements on the microphysical detail is reduced when one considers the change in time at a given location.

To avoid re-computing the scattering behavior of every individual particle, a look-up-table (LUT)

approach is employed by building scattering tables for a selection of particle size distributions, shapes and densities. These tables are then accessed, for every species i, using the bulk mass M_i from WRF and the mean mass-weighted diameter $D_{\mathrm{m},i}$ resulting from the micro-physical assumptions. Three different micro-physical parameterizations (MPP) are considered, viz. Lin [16], WSM6 [11] and ZSH schemes. In the first two MPPs, the diameters $D_{m,i}$ are computed using PSD and mass-size relationships provided in the literature, whereas the radiometric parameters are obtained from a T-matrix code [23]. The third scheme (ZSH), which was derived by the authors by assuming D_m to be related to M through a power law $D_{m,i} = \alpha M_i^{0.17}$ with α a function that varies very slowly in space and time. The scattering LUT is then built assuming Gamma distributions and using DDSCAT, which is based on discrete-dipole approximations [6].

Thus for every record in the WRF "d03" data set, the unattenuated reflectivity $Z_{\mathrm{u},i}(M_i, D_{\mathrm{m},i})$ and the specific attenuation $k_{\mathrm{ext},i}(M_i, D_{\mathrm{m},i})$ provided by the LUT are combined to obtain the equivalent reflectivity

$$Z(\boldsymbol{r}, h) \;=\; \sum_{i=1}^{N_{species}} Z_{\mathrm{u},i}(\boldsymbol{r}, h) \exp\left[-2 \int_{[k,\infty)} \sum_{j=1}^{N_{species}} k_{\mathrm{ext},j}(\boldsymbol{r}, h') dh'\right], \tag{6}$$

with $\boldsymbol{r}$ the geodetic coordinates of the profile and h the height. These radar reflectivities are aggregated horizontally to obtain a $\sim 4.5 \times 4.5\ \mathrm{km}^2$ horizontal resolution similar to GPM DPR, while preserving the original fine vertical sampling of WRF (60 layers between 0 and 20 km). The other WRF output are also averaged to this spatial resolution.

Unless stated otherwise, all the results obtained with all these microphysical schemes are considered equally likely and used together, i.e. as various realizations of the state of the atmosphere. Doing so provides a way of assessing the sensitivity of our simulations and algorithms based on the derivatives of Z. As a result, the data set used in this study comprises 120 instants (every 30 s between 06:00 and 07:00 UTC) for which every scene has 233×233 profiles, each one with 60 vertical bins, and each of these scenes has three realizations of Z corresponding to the three micro-physical schemes.

As an example the maps of vertical averages of the radar reflectivity Z simulated using the WSM6 scheme is displayed in Fig. 6, together with corresponding averages masses of water vapor and condensed water M, and a mask that shows the convective profiles. These maps show the spatial organization of the depression that later became the eye of the hurricane. The convection is mainly present as localized or "popcorn" cells.

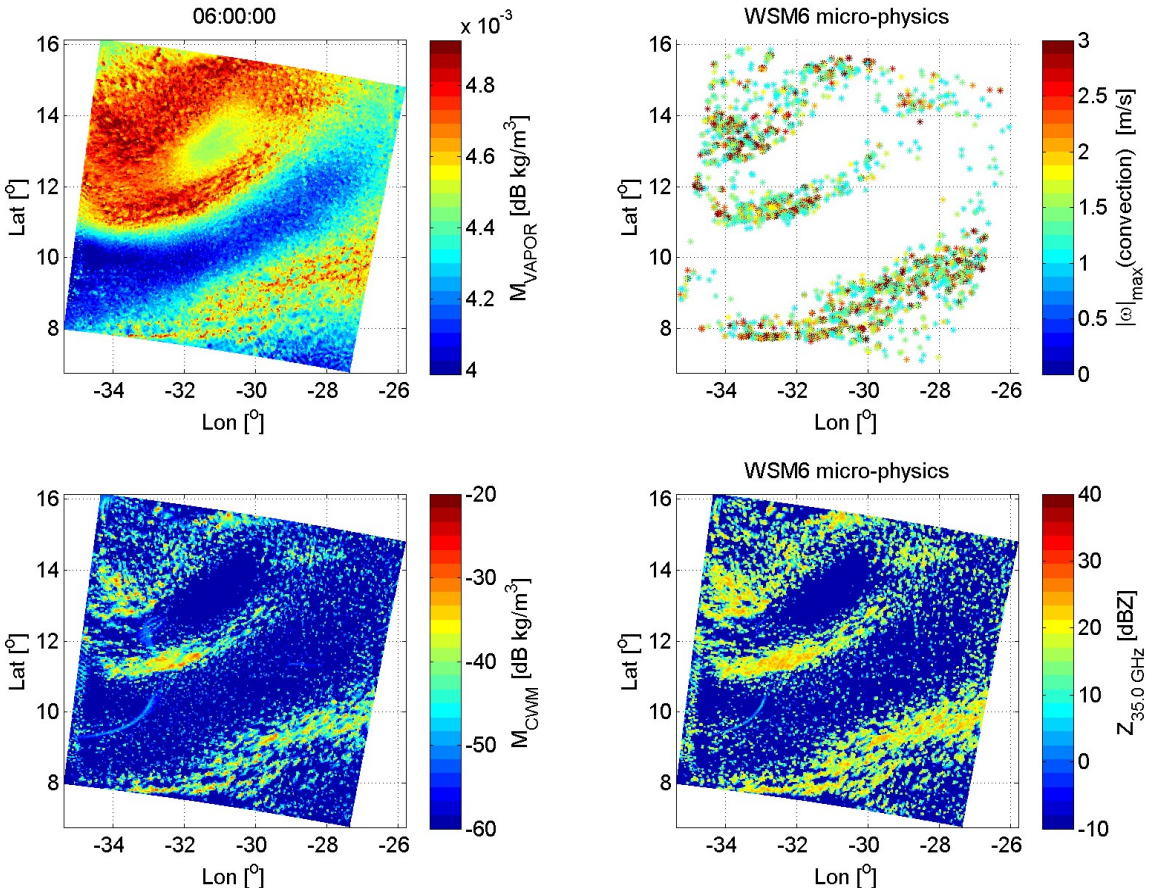

Figure 6: Maps of Isabel simulations at 06:00 UTC: vertically averaged water vapor mass (top left), maximum absolute vertical wind $|\omega|_{\max}$ in convective profiles (top right), CWM (bottom left) and Ka band reflectivity using WSM6 micro-physics (bottom right).

4.2 Comparisons between $Z - M$ and $\Delta_t Z - \Delta_t M$ relationships

It is common in literature to estimate the CWM from the radar measurements via a relation of the form

$$M = aZ^b, \tag{7}$$

with a and b constants [15]. However, universal constants (a, b) that fit all precipitation types at all times and locations do not exist, and retrievals that only use a single frequency suffer from the large variability in space and time of these parameters, particularly a [4]. This large variability is illustrated in Fig. 7, which shows the dispersion in the $Z - M$ relation, as well as maps of $a_{\mathrm{dB}} = 10\log_{10}(a)$ and b obtained by fitting GPM-Core Ka band reflectivity measurements to Level-2 total water contents retrieved from both GPM channels and the passive microwaves. These results correspond to data above an altitude of 4.5 km, to avoid adverse effects caused by

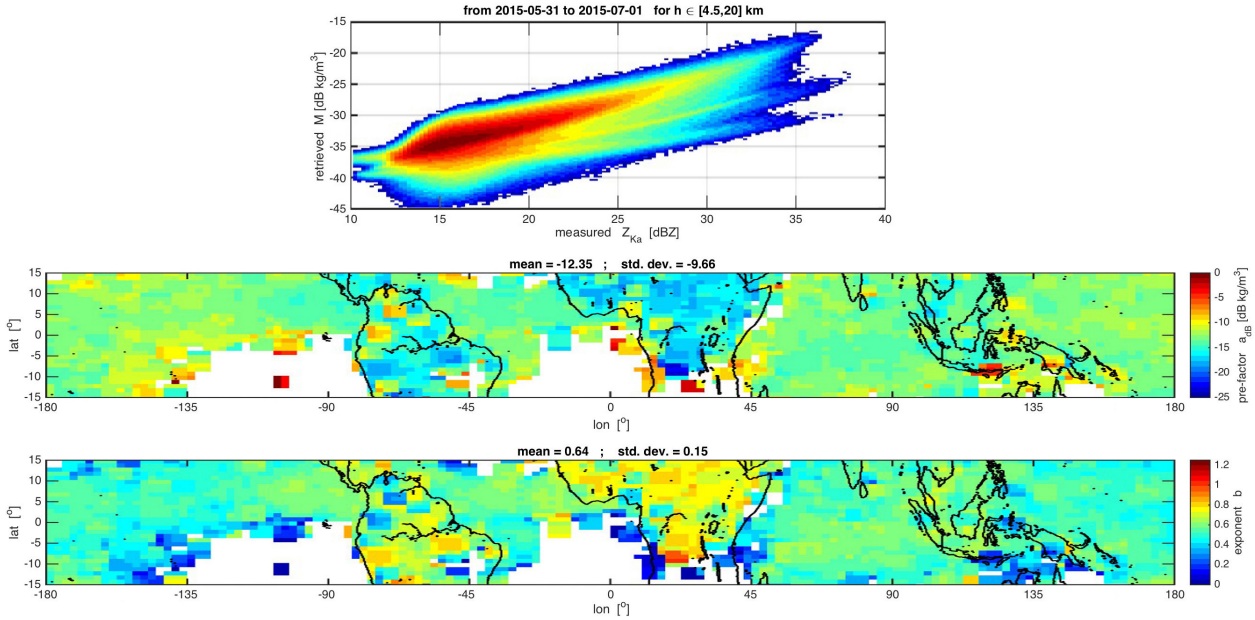

Figure 7: Relation from GPM Ka-band reflectivity measurements (Z) and Level-2 retrieved total water content (M), over the entire month of June 2015 and above 4.5 km: joint distribution of $Z - M$ (top), parameters a_{dB} (second row) and b (bottom row) of a regression $M_{[\mathrm{dBkg/m^3}]} = a_{\mathrm{dB}} + bZ_{[\mathrm{dBZ}]}$.

attenuation and the melting layer on the retrieved CWM. The regressions are applied to regions of size $1.5° \times 1.5°$ for measurements from the entire month of June 2015. While the exponent b remains mostly between 0.6 and 0.8, the largest variations affect a_{dB}.

The large scatter in the $Z - M$ relation is also present in the Isabel simulations as shown in Fig. 8 where the micro-physical parametrizations are either grouped together (top row) or considered

individually (rows below). Similarly to Fig. 7, the Isabel results are analyzed above an altitude

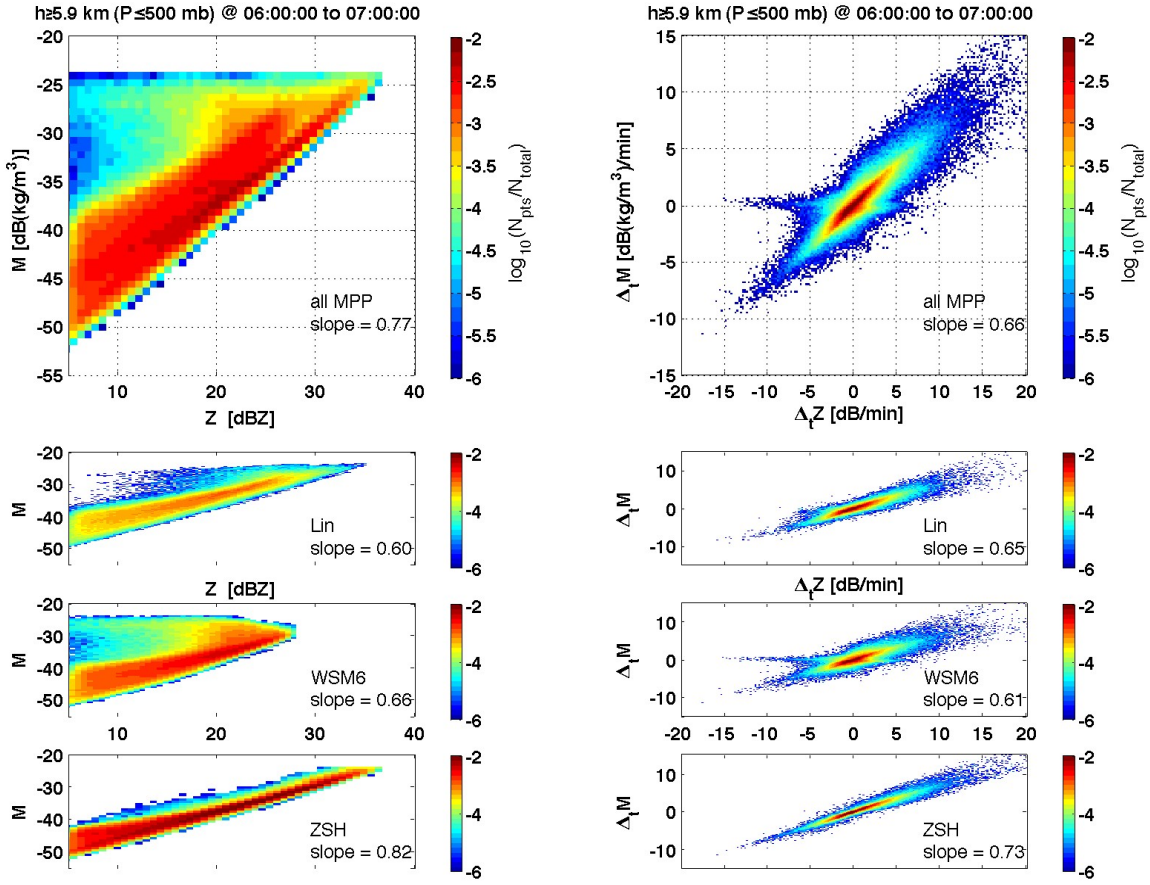

Figure 8: Relationships $Z - M$ (left) and $\Delta_t Z_{[\mathrm{dBZ}]} - \Delta_t M_{[dB]}$ (right) with time differences computed over $\Delta t = 90$ s. Results for all the microphysics grouped together (top) or used individually: Lin (second row), WSM6 (third row) and ZSH (bottom) micro-physics.

of 5.9 km (~ 500 mb level), to avoid the effects of excessive attenuation on the reflectivity. This large variability translates into a prohibitive uncertainty in the retrieved M. For instance, when all the MPP are grouped together (top row, left), there is almost a 20 dB range of uncertainty for the mass corresponding to $Z = 20$ dBZ.

The time derivatives of $Z_{[\mathrm{dBZ}]}$ and $M_{[\mathrm{dB}]} = 10 \log_{10}(M)$ are computed by finite differences over a baseline $\Delta t = 90$ s. Such a short baseline combined the dominantly convective nature of the scene allows to properly estimate the derivatives without accounting for the horizontal advection. The joint distributions of $\Delta_t Z_{[\mathrm{dBZ}]} = \Delta Z_{[\mathrm{dBZ}]}/\Delta t$ and $\Delta_t M_{[\mathrm{dB}]} = \Delta M_{[\mathrm{dB}]}/\Delta t$ are shown in Fig. 8 (right). Remarkably, the uncertainty on $\Delta_t M_{[\mathrm{dB}]}$ retrieved from $\Delta_t Z_{[\mathrm{dBZ}]}$ is considerably smaller than the uncertainty on M. The slope between $\Delta_t M_{[\mathrm{dB}]}$ and $\Delta_t Z_{[\mathrm{dBZ}]}$, i.e. a measure of the exponent b, is robust around ~ 0.7 and largely independent of microphysical assumptions.

As explained in Section 2, the robustness of the $(\Delta_t M_{[\mathrm{dB}]}, \Delta_t Z_{[\mathrm{dBZ}]})$ relation stems from the fact that, on time scales of order 30–120 seconds and above the freezing level, biases inherent in $Z - M$ relationships that produce a large spread cancel when data are differentiated over short time intervals (tens of seconds). Thus, the computed $\Delta_t Z_{[\mathrm{dBZ}]}$ provides a reliable measure of the moistening rate of the upper troposphere.

4.3 Vertical air mass fluxes: relation to $\Delta_t Z$ and Bayesian retrievals

We now demonstrate that pairs of radar measurements and their derivatives contain unique information about vertical transport of air in convective cores. To this end a canonical-correlations analysis (CCA) is combined with a principal-component decomposition to identify correlations between radar measurements and vertical fluxes of air masses. A Bayesian algorithm is then described to estimate the vertical fluxes of dry and moist air in convection from the radar observations. These retrieved results can then be scaled relative to the total amount of convection by using passive-microwave measurements.

Given two observation times t and $t + \Delta t$, we denote the corresponding radar observations $Z_{\mathrm{PRE}}(\cdot, \cdot, t) = Z_{[\mathrm{dBZ}]}(\cdot, \cdot, t)$ and $Z_{\mathrm{POST}}(\cdot, \cdot, t) = Z_{[\mathrm{dBZ}]}(\cdot, \cdot, t + \Delta t)$ and define the time-average and -difference as $Z_{\mathrm{AVG}} = (Z_{\mathrm{AVG}} + Z_{\mathrm{POST}})/2$ and $\Delta_t Z_{[\mathrm{dBZ}]} = (Z_{\mathrm{POST}} - Z_{\mathrm{AVG}})/\Delta t$, respectively. The net mass of dry air transported vertically between times t and $t + \Delta t$ through the profile $\boldsymbol{r}$ at the altitude $h \geq 0$ is measured via the flux

$$Q_{\mathrm{AIR}}(\boldsymbol{r}, h, t) \;=\; \int_t^{t+\Delta t} \rho_{\mathrm{AIR}}(\boldsymbol{r}, h, t')\omega(\boldsymbol{r}, h, t')dt' \qquad [\mathrm{kg} \cdot \mathrm{m}^{-2}]. \tag{8}$$

The flux of moist air Q_{CWM} is defined similarly by substituting M for ρ_{AIR} in Eq. (8). While the radar products Z_{AVG} and $\Delta_t Z_{[\mathrm{dBZ}]}$ only use observations at times t and $t + \Delta t$ in the upper troposphere ($h \geq 5$ km), the flux Q_{AIR} is defined using contributions from $\rho_{\mathrm{AIR}}\omega$ at all intermediate times between t and $t + \Delta t$ and over the entire profile ($h \geq 0$). The set $\mathcal{C}_t$ of convective profiles at time t gathers the profiles that contain at least five bins with $Z_{[\mathrm{dBZ}]} \geq 5$ dBZ and at least one bin with a vertical wind $|\omega| \geq 1 \ \mathrm{m} \cdot \mathrm{s}^{-1}$. The set of all convective profiles between 06:00 and 07:00 UTC is denoted $\mathcal{C} = \{\mathcal{C}_t\}_{06:00 \leq t \leq 07:00 \ \mathrm{UTC}}$.

4.3.1 Principal-component and canonical-correlation analyses

Focusing on the convective profiles in $\mathcal{C}$, a principal-component analysis (PCA) is applied to Z_{AVG}, $\Delta_t Z_{[\mathrm{dBZ}]}$ and Q_{AIR}. This allows to project the initial fields, e.g. Q_{AIR}, on the basis of

principal vectors $\{\boldsymbol{\varphi}_{\mathrm{Q},k}\}_{k=1,\ldots,N_0}$ as follows

$$Q_{\mathrm{AIR}}(\boldsymbol{r},h,t) \;=\; \sum_{k=1}^{N_0} \eta_{\mathrm{Q},k}(\boldsymbol{r},t)\varphi_{\mathrm{Q},k}(h), \qquad \forall h \geq 0 \text{ km}, \tag{9}$$

where $N_0 = 60$ is the number of bins in the entire vertical profile. The principal components (PC) $\{\eta_{\mathrm{Q},k}\}_{k=1,\ldots,N_0}$ are mutually uncorrelated with variances equal to the sorted eigenvalues $\{\lambda_{\mathrm{Q},k}\}_{k=1,\ldots,N_0}$. Similarly, Z_{AVG} and $\Delta_t Z_{[\mathrm{dBZ}]}$ are expressed in terms of their eigen-systems denoted $\{\lambda_{\mathrm{A},k},\boldsymbol{\varphi}_{\mathrm{A},k}\}_{k=1,\ldots,N_1}$ and $\{\lambda_{\mathrm{D},k},\boldsymbol{\varphi}_{\mathrm{D},k}\}_{k=1,\ldots,N_1}$, respectively. The rapid decay of the eigenvalues allows to approximate the initial fields using the first few PCs, while capturing the variability of the initial fields. For instance, Table 1 shows that the first four PCs of Q_{AIR} and Z_{AVG} already represent more than 90% of the total variability. For $\Delta_t Z_{[\mathrm{dBZ}]}$, which has a less smooth spectrum, the first six PCs still represent more than 70% of the total variability.

Table 1: Relative weights of the first principal components of Q_{AIR}, Z_{AVG} and $\Delta_t Z_{[\mathrm{dBZ}]}$ from all convective profiles in the Isabel simulations.

	Relative weight of the first M eigenvalues, i.e. $\sum_{k=1}^{M}\lambda_k \Big/ \sum_{k=1}^{\infty}\lambda_k$							
	$M=1$	$M=2$	$M=3$	$M=4$	$M=5$	$M=6$	$M=7$	$M=8$
Q_{AIR}	0.44	0.72	0.85	0.92	0.95	0.97	0.98	0.99
Z_{AVG}	0.52	0.81	0.90	0.94	0.97	0.98	0.99	0.99
$\Delta_t Z_{[\mathrm{dBZ}]}$	0.24	0.40	0.53	0.62	0.69	0.74	0.78	0.81

Figure 9 shows the profiles of the first three eigenvectors of all the fields. These profiles indicate the combinations of the initial fields that produce the largest variability in space and time. For instance, the first principal vector $\boldsymbol{\varphi}_{\mathrm{A},1}$ corresponds to a weighted average of Z_{AVG} above 5 km, with an emphasis around ~ 8 km, whereas $\boldsymbol{\varphi}_{\mathrm{A},2}$ is a weighted difference between $Z_{\mathrm{AVG}}(h \geq 8 \text{ km})$ and $Z_{\mathrm{AVG}}(h \in [5,8] \text{ km})$. A similar structure can be seen in the eigenvectors of the dry air flux, where $\boldsymbol{\varphi}_{\mathrm{Q},1}$ averages Q_{AIR} mainly around 5 km and $\boldsymbol{\varphi}_{\mathrm{Q},2}$ makes the difference between $Q_{\mathrm{AIR}}(h \geq 5 \text{ km})$ and $Q_{\mathrm{AIR}}(h < 5 \text{ km})$. The eigenvectors of $\Delta_t Z_{[\mathrm{dBZ}]}$ have different patterns as $\boldsymbol{\varphi}_{\mathrm{D},1}$ is an average of $\Delta_t Z_{[\mathrm{dBZ}]}(h \in [5,10] \text{ km})$ corrected by the average of $\Delta_t Z_{[\mathrm{dBZ}]}(h \geq 10 \text{ km})$, and conversely $\boldsymbol{\varphi}_{\mathrm{D},2}$ is an average of $\Delta_t Z_{[\mathrm{dBZ}]}(h \geq 7 \text{ km})$ corrected by the average of $\Delta_t Z_{[\mathrm{dBZ}]}(h \in [5,7] \text{ km})$.

Next, a canonical-correlation analysis (CCA) is applied to identify the linear combinations of the radar observations that are most correlated with components of Q_{AIR} [12]. The details of our implementation of this statistical method are provided in Appendix B. As a result we obtain a set of CCA projectors,

$$\boldsymbol{\psi}_{\mathrm{A},j}(h) = \sum_{k=1}^{M_1} a_{k,j}\varphi_{\mathrm{A},k}(h), \;\; \boldsymbol{\psi}_{\mathrm{D},j}(h) = \sum_{k=1}^{M_2} a_{M_1+k,j}\varphi_{\mathrm{D},k}(h) \text{ and } \boldsymbol{\psi}_{\mathrm{Q},j}(h) = \sum_{k=1}^{M_0} b_{k,j}\varphi_{\mathrm{Q},k}(h), \tag{10}$$

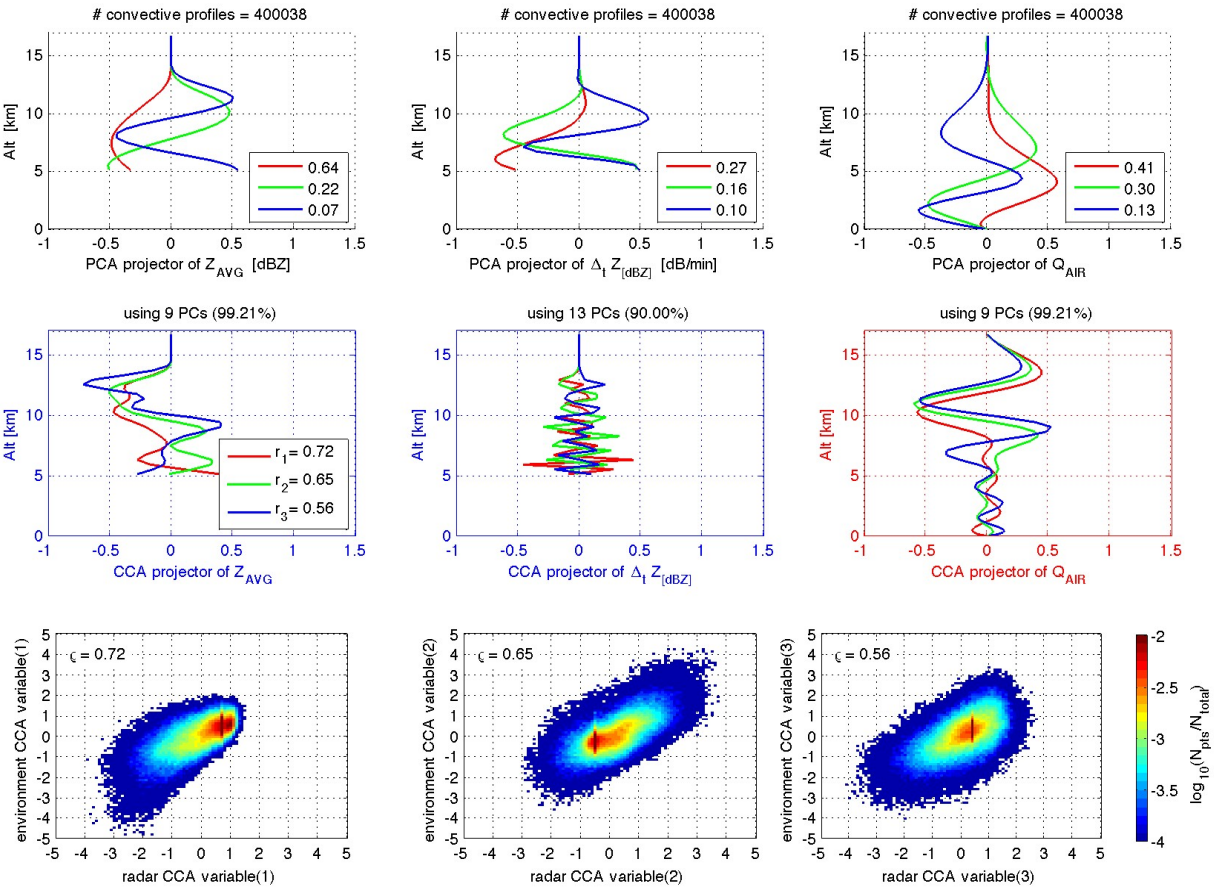

Figure 9: Principal-component (PCA) and canonical-correlation analyses (CCA) of convective profiles in Isabel: vertical profiles of principal vectors (top) for $Z_{\rm AVG}$ (left), $\Delta_t Z_{\rm [dBZ]}$ (middle) and $Q_{\rm AIR}$ (right), with normalized eigenvalues in legend; vertical profiles of CCA weighting vectors (second row) for $Z_{\rm AVG}$ (left), $\Delta_t Z_{\rm [dBZ]}$ (middle) and $Q_{\rm AIR}$ (right), with CCA correlation coefficient in legend; joint distributions of first (left), second (middle) and third (right) CCA pairs of variables (bottom row).

that define the CCA variables

$$v_j(\boldsymbol{r},t) = \int_0^\infty Q_{\rm AIR}(\boldsymbol{r},h,t)\boldsymbol{\psi}_{{\rm Q},j}(h)dh, \tag{11a}$$

$$\text{and} \qquad u_j(\boldsymbol{r},t) = u_{{\rm A},j}(\boldsymbol{r},t) + u_{{\rm D},j}(\boldsymbol{r},t), \tag{11b}$$

$$\text{with} \qquad u_{{\rm A},j}(\boldsymbol{r},t) = \int_5^\infty Z_{\rm AVG}(\boldsymbol{r},h,t)\boldsymbol{\psi}_{{\rm A},j}(h)dh, \tag{11c}$$

$$u_{{\rm D},j}(\boldsymbol{r},t) = \int_5^\infty \Delta_t Z_{\rm [dBZ]}(\boldsymbol{r},h,t)\boldsymbol{\psi}_{{\rm D},j}(h)dh. \tag{11d}$$

The cefficients $\{a_{k,j}\}_{k,j}$ and $\{b_{k,j}\}_{k,j}$ are provided by the CCA algorithm. By construction, the

pairs of CCA variables (u_j, v_j) are sorted by decreasing levels of statistical correlation. This is illustrated in Fig. 9 (bottom), which shows the scatterplot of the first three pairs of CCA variables and the correlation levels dropping from 72% for (u_1, v_1) to 65% for (u_2, v_2) and 56% for (u_3, v_3). All these are significant levels of correlation. The profiles of the corresponding CCA projectors (second row) differ from those of the principal vectors. Interestingly, even though the entire profile of $Q_{\rm air}$ is used in the analysis, the strongest contributions in $\boldsymbol{\psi}_{{\rm Q},j}$ correspond to altitudes above 5 km where the radar observations are available. The frequent changes in the signs of $\boldsymbol{\psi}_{{\rm D},j}$ make it difficult to interpret the patterns of these vectors. Conversely, we see from $\boldsymbol{\psi}_{{\rm Q},1}$ and $\boldsymbol{\psi}_{{\rm A},1}$ that the difference between the dry air transported above 8 km and the dry air transported below 8 km is strongly related to a weighted average of the reflectivity $Z_{\rm AVG}$ around 7, 10 and 13 km.

4.3.2 Bayesian retrieval of vertical mass fluxes

While the results in Fig. 9 confirm the significant correlation between profiles of radar observations and vertical mass fluxes, the scatter in the joint distributions of CCA variables indicates that there is more to the dependency of $Q_{\rm AIR}$ on $Z_{\rm AVG}$ and $\Delta_t Z_{\rm [dBZ]}$ than simple linear relationships between CCA variables. Thus, to estimate the profile of $Q_{\rm AIR}$ from $Z_{\rm AVG}$ and $\Delta_t Z_{\rm [dBZ]}$, we use a Bayesian-interpolation approach conditioned by $Z_{\rm AVG}$.

First, the ranges of the dominant PCs of $Z_{\rm AVG}$ are divided into sub-domains. To obtain a grid with a manageable size, an importance-sampling strategy is used, i.e. the range of $\eta_{{\rm A},k}$ is divided according to the weight of its eigenvalue into $N_k = \lceil 10\lambda_{{\rm A},k}/\lambda_{{\rm A},1} \rceil + 1$ sub-domains. In the present case, this implies $N_1 = 11$, $N_2 = 7$, $N_3 = 3$ and $N_4 = N_5 = N_6 = 2$. Then, given a cell $\mathcal{A}_0$ in the resulting hyper-cube, we determine all the corresponding samples (i.e. $\mathcal{C}_0 = \eta_{\rm A}^{-1}(\mathcal{A}_0) \subset \mathcal{C}$) and use these samples (i.e. $\{\eta_{{\rm D},k}\}_{k=1,\ldots,M_2}(\mathcal{C}_0)$ and $\{\eta_{{\rm Q},k}\}_{k=1,\ldots,M_0}(\mathcal{C}_0)$) to interpolate every component of $\{\eta_{{\rm Q},k}\}_{k=1,\ldots,M_0}$ individually in terms of all the components of $\{\eta_{{\rm D},k}\}_{k=1,\ldots,M_2}$. [1] A first-order polynomial interpolation is used (we have verfied that higher-order interpolations yielded limited improvement). By repeating the process for every cell of the hypercube, we obtain an approximation for the PCs of $Q_{\rm AIR}$, which are denoted $\{\widehat{\eta_{{\rm Q},k}}\}_{k=1,\ldots,M_0}$ and used in Eq. (9) to approximate $Q_{\rm AIR}$ by

$$\widehat{Q_{\rm AIR}}(\boldsymbol{r}, h, t) \;\approx\; E_{\rm Q}(h) + \sum_{k=1}^{M_0} \widehat{\eta_{{\rm Q},k}}(\boldsymbol{r}, t)\varphi_{{\rm Q},k}(h). \tag{12}$$

The accuracy of this retrieval algorithm is illustrated in Fig. 10 (left columns), which shows the joint distribution of the retrieved $Q_{\rm AIR}$ versus the model truth. These quantities are averaged over 100-mb-thick layers. Indeed, we observe the strong correlation ($\geq 75\%$) between the estimated

[1] In fact, we use $\{\eta_{{\rm D},k}\}_{k=1,\ldots,M_1}(\mathcal{C}_0)$ and $\{v_j\}_{j=1,\ldots,M_0}(\mathcal{C}_0)$ and interpolate every component of $\{v_j\}_{j=1,\ldots,M_0}$ individually in terms of all the components of $\{\eta_{{\rm D},k}\}_{k=1,\ldots,M_1}$. Then, we pseudo-invert the matrix of CCA coefficients to obtain $\eta_{{\rm Q},k}\}_{k=1,\ldots,M_0}$ from $\{v_j\}_{j=1,\ldots,M_0}$.

and true fluxes of dry air. The same retrieval algorithm is applied to the flux of moist air Q_{CWM} and yields equally accurate results as can be seen in Fig. 10 (right).

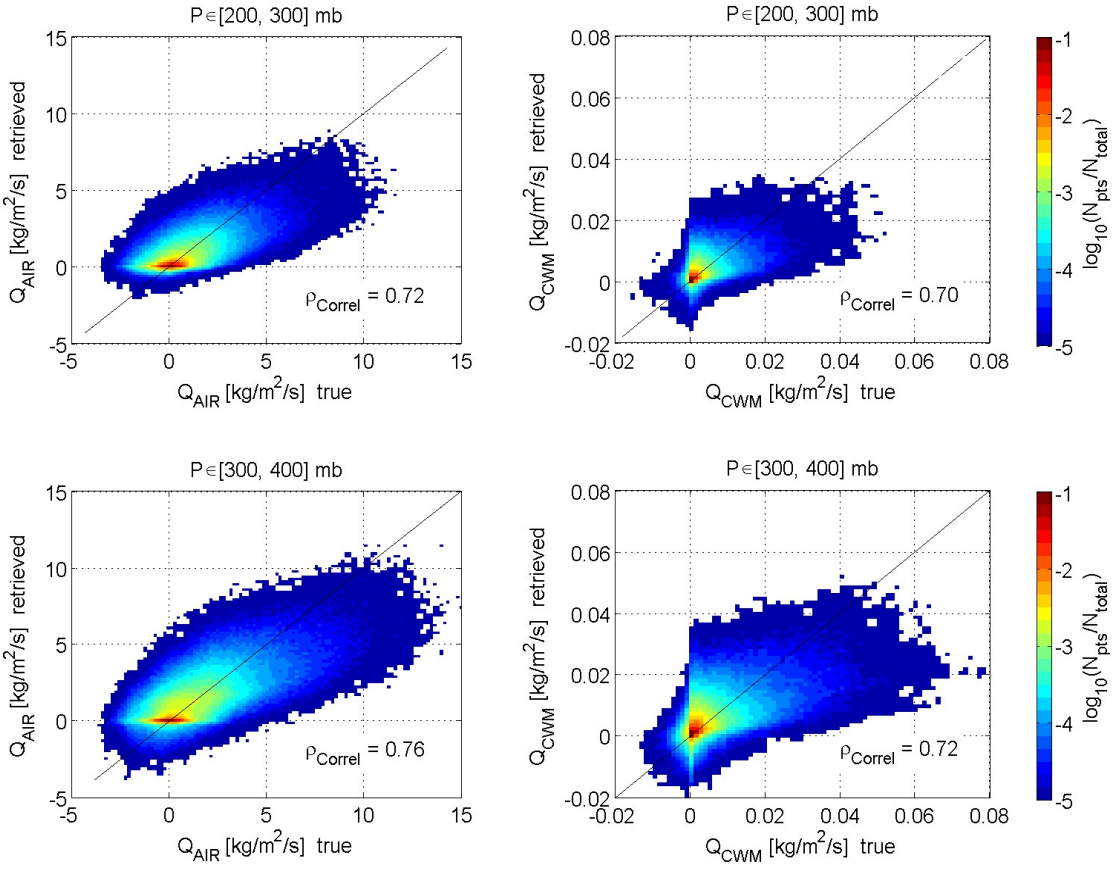

Figure 10: Results of Bayesian retrievals of dry- (left) and moist- (right) air fluxes Q_{AIR} and Q_{CWM} versus model truths. The Fluxes are averaged vertically over [200,300] mb (top) and [300,400] mb (bottom).

The accuracy of the retrievals is also apparent in the CFADs of the retrieved mass fluxes compared to those of the true fluxes. Figure 11 shows the nearly perfect restitution of the mean and median (50%) profiles of Q_{AIR} and Q_{CWM}. The dynamic range of the fluxes (indicated by difference between 20% and 80% quantiles) is also well estimated despite the slight underestimation of lower values of Q_{AIR} and the underestimation of the largest values of Q_{CWM} below 7.5 km.

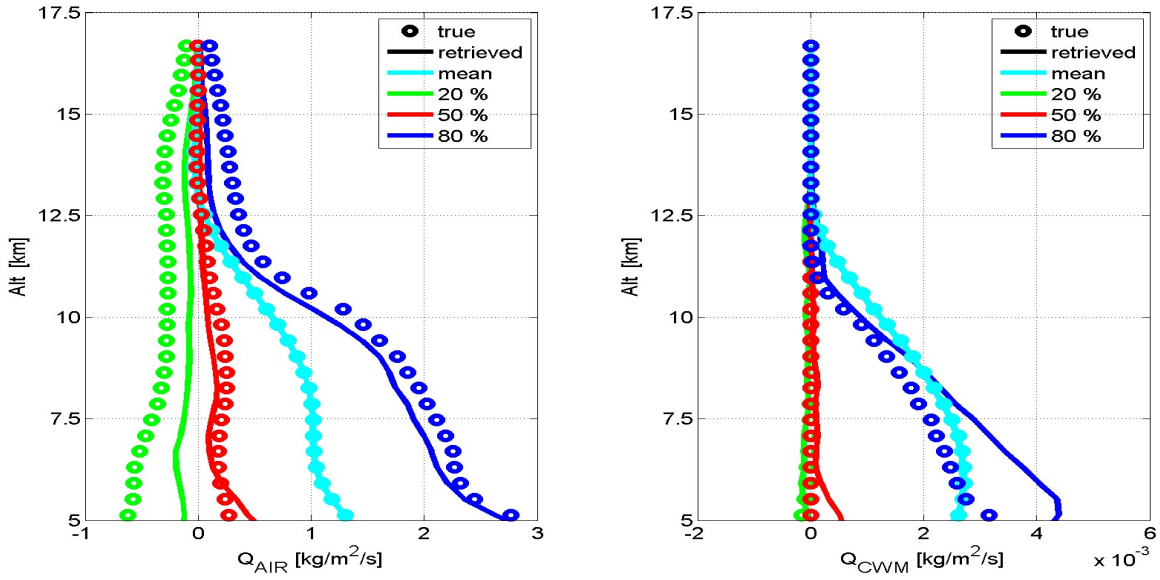

Figure 11: Statistical comparison between retrieved air mass fluxes and model truths: CFAD of dry-air flux (left) and moist-air flux (right).

4.4 Scaling of results in convection

For numerical weather models to fully benefit from the retrieved convective fluxes, these must be scaled relative to the total amount of convection in the tropics. Indeed, due to their narrow swaths, spaceborne radars can only observe a limited portion of the tropics.

For this purpose, the large fleet of wide-swath radiometers in LEO is particularly valuable as it warrants a frequent revisit time in the tropics. For instance, the GPM-era constellation of mm-wave sounders revisits every point in the tropic at least 18 times daily. While the measured brightness temperatures do not resolve the vertical structure of precipitation, they are sensitive to different heights of the atmosphere depending on the frequency of the instrument. The various passive measurements can be combined to build estimators for the vertically integrated water content of the atmosphere and therewith the depth of convection.

This capability is illustrated in Fig. 12 using the WRF data at at 06:00 UTC and WSM6 scattering tables in the Successive Order of Interaction (SOI) radiative-transfer model [10] to simulate brightness temperatures. The simulated channels are those of the Microwave Humidity Sounder (MHS), i.e. $T_{89,V}$, $T_{157,V}$, $T_{183.311\pm1,H}$, $T_{183.311\pm3,H}$ and $T_{190.311,V}$ with H (V) indicating a horizontal (vertical) polarization. By applying a CCA to the first four PCs of the condensed water mass M and the measured brightness temperatures, an estimator is built for the M. The maps

in Fig. 12, show the high correlation between this estimator (right) and the vertically integrated CWM (left).

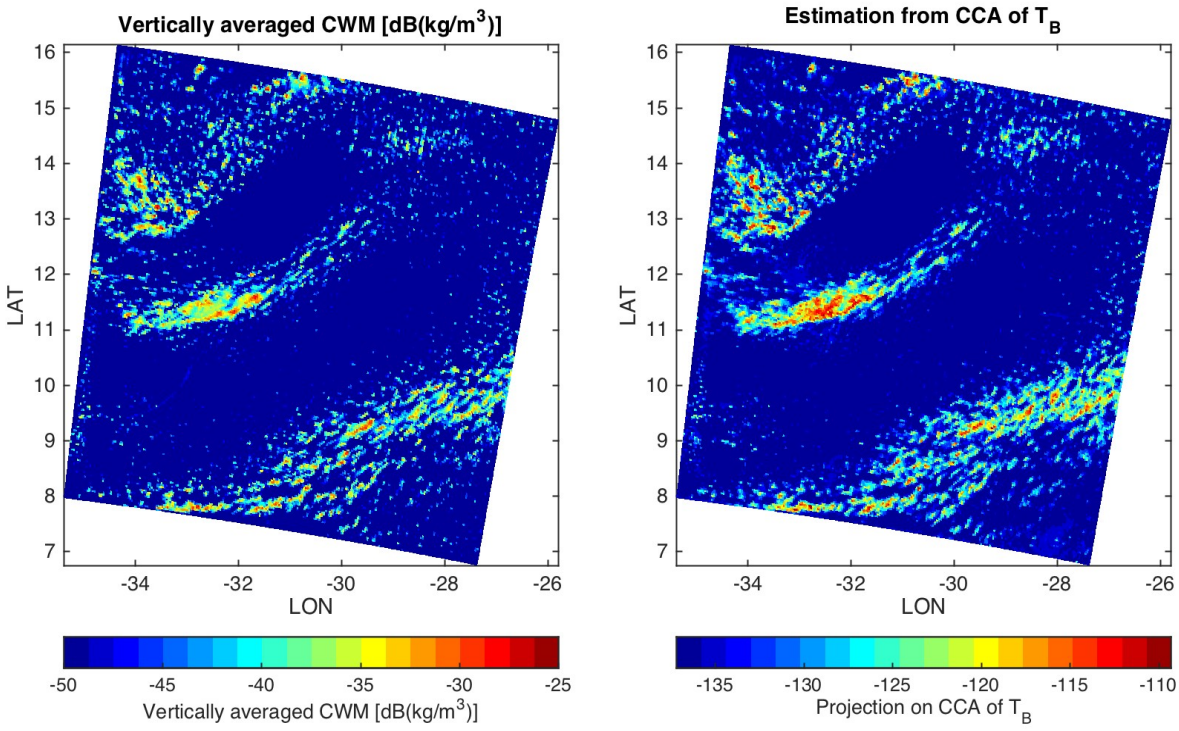

Figure 12: Comparison between vertically averaged CWM M (left) from Isabel simulations at 06:00:00, and our proxy for CWM (right) consisting of the optimally correlation combination of MHS brightness temperatures determined from the statistics that we calculated from our simulation using WSM6 microphysics.

5 Application to a convoy of satellites

Given the long revisit time of low-Earth orbiting satellites, the only way to gather frequent radar observations with a sufficient time resolution to enable the analysis proposed in this article consists in using multiple spacecraft. The idea is to acquire the atmospheric measurements using a convoy of satellites that trail each other by a short time Δt. Such a concept can be implemented

in practice owing to recent advances in small-satellite technologies that allow to deploy multiple CubeSats on the same orbit in one launch at a reasonable financial cost. Equally important are the advances made in electronic hardware and signal processing techniques to miniaturize radars and qualify them for spaceborne missions. One such example is the novel Radar in a CubeSat (RainCube) technology developed at JPL (see artist concept in Fig. 13) and selected for demonstration in space by NASA through its In-Space Validation of Earth Science Technologies (INVEST) program [17].

Figure 13: Artist's concept of RainCube.

For our concept study, we consider a train of two such satellites separated by a given time Δt and each embarking a "Mini nadir-pointing Ka-band Atmospheric Radars" (miniKaAR) that use the RainCube technology. The characteristics of miniKaAR are summarized in Table 2. With a horizontal resolution of 5 km and a vertical sampling of 250 m, the measurements of this instrument will have a strong synergy with the dual-frequency radar of the GPM Core satellite. We analyze the impact of some of the hardware and operational design parameters on the accuracy to be expected from a time-differenced analysis, and conversely the design constraints imposed by the performance thresholds of our radar analysis.

5.1 Effect of the sensitivity in reflectivity

The cumulative distribution function of the reflectivity factors in the convective cores of our Isabel simulations (from 06:00 to 07:00 UTC and using all micro-physics) is computed and plotted as a function of height in Fig. 14. This figure whos that given its 17 dBZ sensitivity,

Table 2: Characteristics of miniKaAR.

miniKaAR Characteristics	Estimate
Mass	21 kg
Volume Dimensions	$10 \times 20 \times 20$ cm^3
Antenna size	95 cm
Frequency	35.75 GHz
Peak transmit power	10 W
Spatial Resolution	5 km
Range Resolution	250 m
Measurement sensitivity	17 dBZ
Measurement precision	1 dBZ

MiniKaAR should be able to observe more than 70 % of all Ka-band reflectivities between 4.5 and 9 km. As expected, the returns below 4.5 km should be strongly affected by attenuation, while the hydrometeors in the upper troposphere (above 10 km) should produce relatively weak echoes.

5.2 Optimal inter-radar separation

To investigate the effect of the time spacing between the two spacecraft of the convoy, we consider different time delays, viz. $\Delta t \in \{30 \text{ s}, 60 \text{ s}, 90 \text{ s}, 240 \text{ s}\}$ and compute the CFADs of absolute changes in $Z_{[\text{dBZ}]}$, which are plotted in Fig. 15 (bottom). Moreover, to measure the non-stationarity of Q_{air}, we compute the maximum relative variation of Q_{avg} as a function of Δt using the ratio

$$r_Q(\boldsymbol{r}, h, \delta t) \quad = \quad \frac{\max_{\Delta t \leq \delta t}[Q_{\text{avg}}(\boldsymbol{r}, h, \Delta t)] - \min_{\Delta t \leq \delta t}[Q_{\text{avg}}(\boldsymbol{r}, h, \Delta t)]}{\mathbb{E}_{\Delta t \leq \delta t}\left[|Q_{\text{avg}}(\boldsymbol{r}, h, \Delta t)|\right]}, \tag{13}$$

with $\boldsymbol{r}$ the convective profile coordinates and h the height. For instance, $r_Q(\boldsymbol{r}, h, \delta t' = 60 \text{ s})$ measures the relative variation of Q_{air} in profile $\boldsymbol{r}$ at the altitude h as it is computed for $\Delta t = 30$ s and $\Delta t = 60$ s.

The CDF of r_Q plotted in Fig. 15 (top) shows that with a separation of 240 s, more than 50% of all convective columns have a maximum variability that exceeds 150%. Thus, such a separation would not yield useful measurements as the target Q_{AIR} that we want to estimate would have varied by 150% or more. This statistic improves significantly for shorter separations, since for $\Delta t \leq 60$ s, 80% of all convective columns have a maximum variability that is smaller than 50%. However, for $\Delta t \leq 60$ s, Fig. 15 (bottom) shows that 50% of all columns also have a reflectivity difference that is below the 1 dBZ precision of MiniKaAR. Thus, the 90 seconds separation is a compromise between sensitivity threshold to the change in reflectivity and the stationarity of the dynamical variables during the time interval.

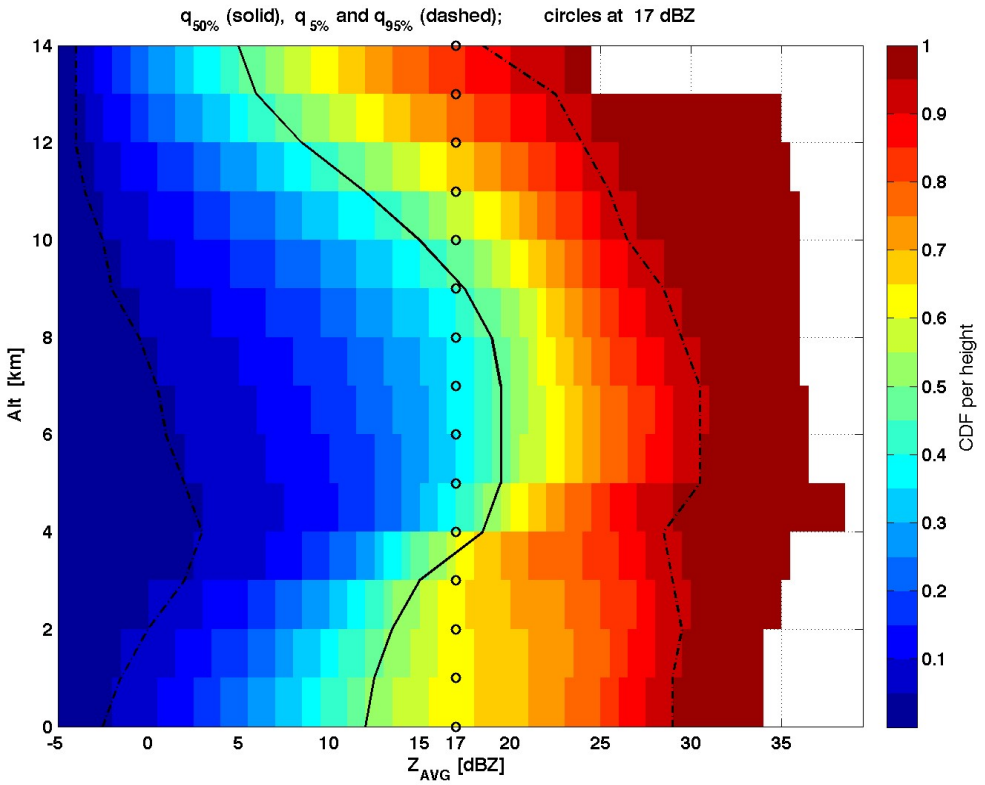

Figure 14: CDF-by-altitude diagram of simulated miniKaAR reflectivity factors (with all three micro-physics) for columns where $|\omega| \geq 1 \text{ m} \cdot \text{s}^{-1}$.

5.3 Sensitivity to pointing uncertainties

Pointing uncertainties must be accounted for since the analysis presented in this article depends crucially on the two spacecraft's ability to observe the same atmospheric region. We tackle this issue by gradually injecting mismatches between beam pairs and tracking their effects on the correlation between the mass rate of change $\Delta_t M/M$ and the commputed $\Delta Z_{[\text{dBZ}]}$ from mismatched beams. Figure 16 illustrates the progressive degradation of the relation between the measured reflectivity difference and the estimated rate-of-change of the mass that results from a progressively greater degradation in the coincidence between the two beams, from our simulations. The correlation between $\Delta_t M$ and $\Delta Z_{[\text{dBZ}]}$ goes from 86% when the beams coincide perfectly (top left), to 81% (74%) when the overlap decreases to 78% (67%) (bottom row).

In terms of the uncertainty induced on the estimated mass rate, Figure 17 shows this degradation

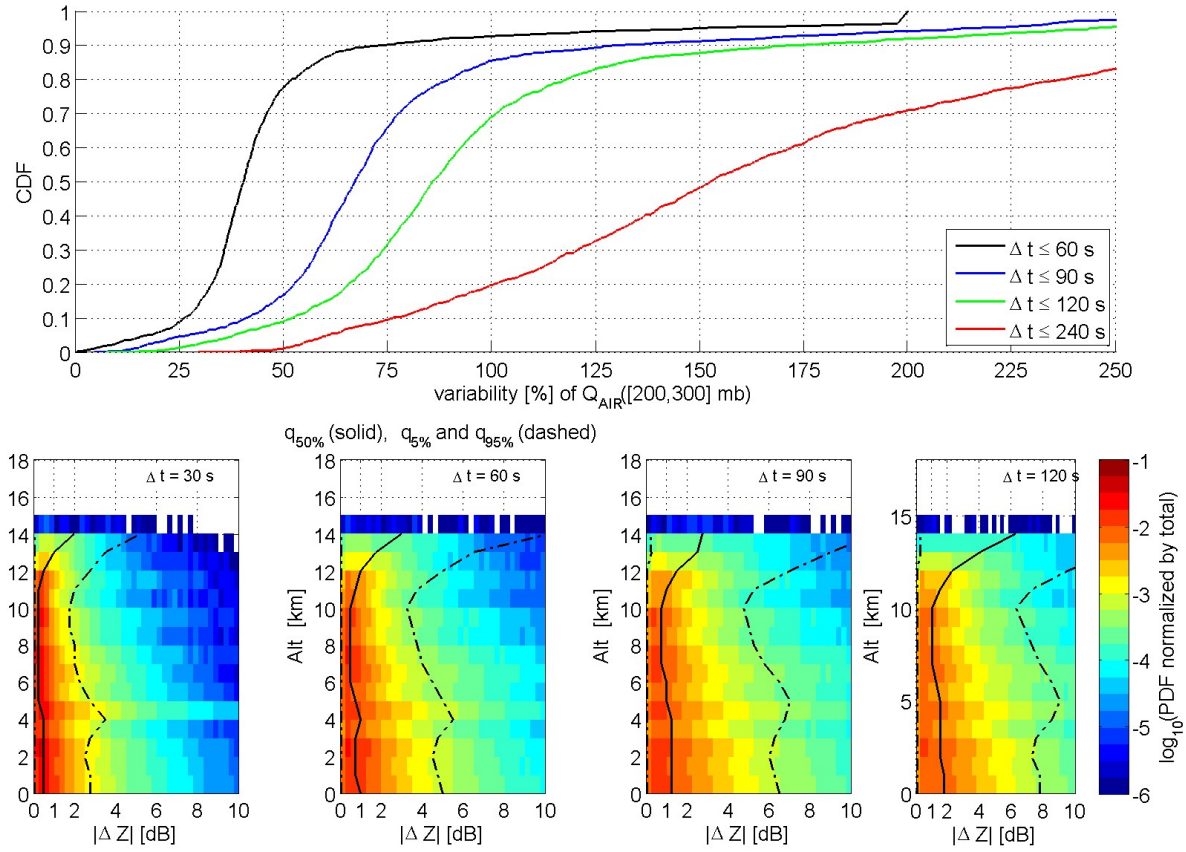

Figure 15: CDF of the stationarity ratio r_Q of Q_{AIR} for time separations of 60 s, 90 s, 2 min and 4 min and computed over convective columns (top). CFAD of the absolute variation in reflectivity over durations of 30 s, 60 s, 90 s, 2 min and 4 min and computed over convective columns (bottom).

as a function of the fractional overlap between the two beams, as we derived it from our cloud-resolving simulations. A decrease of the fractional overlap to 82% increases the r.m.s uncertainty to 0.55, i.e., an increase of 10%. We required this to be the maximum increase in uncertainty due to pointing. This lower bound on the fractional overlap is equivalent to requiring that the difference in the pointing angles (from an altitude of 500 km) should not exceed about 0.1 degrees. Since the pointing errors on the two beams are independent, this can be enforced by requiring the two-sigma error on each beam to be smaller than 0.05 degrees (so that even if the errors move the two beams in exactly opposite directions, the difference will still not exceed 0.1 degrees). This implies a required 1-sigma uncertainty of 0.025 degrees.

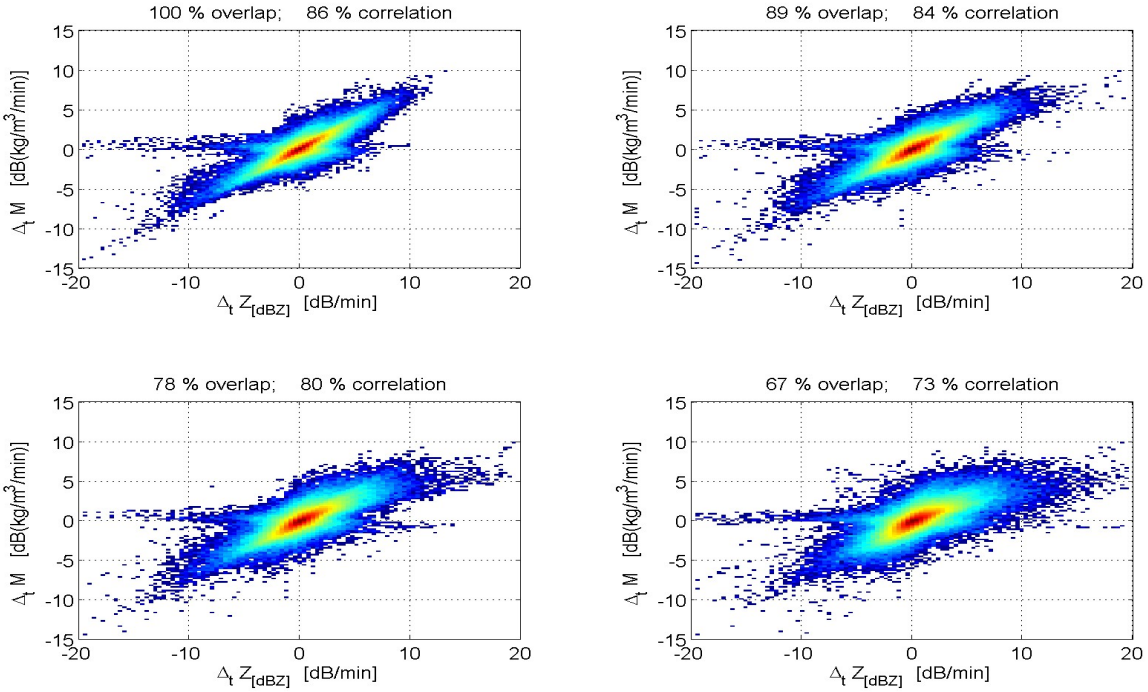

Figure 16: Effect of pointing uncertainties on $\Delta_t Z_{[\mathrm{dBZ}]} - -\Delta_t M$ relationship: with 100% (top left), 89% (top right), 78% (bottom left) and 67% (bottom right) overlap between beams of two miniKaAR radars.

6 Conclusions

This article has presented a novel technique to characterize dynamic atmospheric processes by using frequently-acquired tri-dimensional radar reflectivity measurements from low-Earth orbiting satellites. Starting with ground-based NEXRAD data, we have shown the added value of time derivatives of the radar measurements, (possibly adjusted for advection estimated using a digital-image-correlation technique). The derived products complement and refine the information provided by the radar reflectivity factors by highlighting regions of increasing/decreasing moisture in extreme-weather events such as blizzards of cyclones. The computed derivatives also reveal latent features that are otherwise invisible in the radar reflectivities, such as the evidence of water vapor provided by the atmospheric river that was concomitant with the California Blizzard of January 2008.

Using a large set of high-resolution numerical-weather simulations from WRF, we have shown the robustness of the $d_t Z_{[\mathrm{dBZ}]} - d_t M/M$ relationship between derivatives of the reflectivity and the rate of change of condensed-water mass in the upper atmosphere (above 500 mb). The

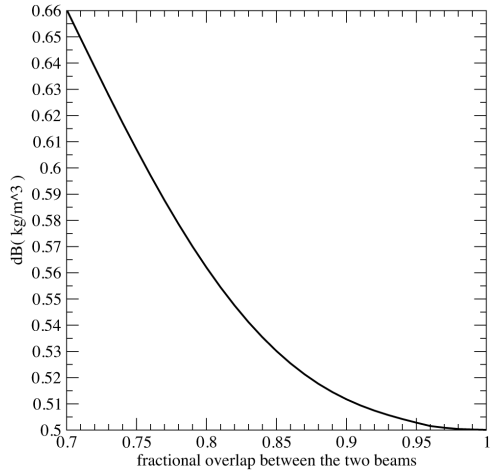

Figure 17: Effect of pointing uncertainties on $\Delta_t Z_{[\mathrm{dBZ}]} - -\Delta_t M$ relationship: with 100% (top left), 89% (top right), 78% (bottom left) and 67% (bottom right) overlap between beams of two miniKaAR radars.

robustness of the $d_t Z_{[\mathrm{dBZ}]} - d_t M/M$ relation, which is independent from the micro-physical assumptions of the radiative transfer simulations, provides reliable estimates of the moistening rate of the upper atmosphere, which can in turns be used to nudge numerical models. This is in contrast with the large noisiness of single-frequency $Z - M$ relationships, as evidenced using level-2 GPM products.

The fine vertical resolution of our simulations allowed us to resolve vertical air mass transports in tropical convective cores. By combining a principal-component analysis with a canonical-correlation analysis, we have shown the significant correlation that exists in the upper atmosphere between the radar observations and their derivatives on the one hand, and vertical fluxes of moist and dry air on the other hand. Furthermore, we implemented a Bayesian retrieval algorithm to restitute mass fluxes with a high degree of accuracy, i.e. with more than 70% correlation between the estimates and their model truths, and a nearly perfect restitution of the mean and envelope of the vertical profiles of Q_{AIR} and Q_{CWM} in convection. The thus obtained information could help improve the parametrization of dynamic atmospheric processes such as detrainment, for which there is a large uncertainty in current models. Moreover, we showed that these estimates can be scaled for use in numerical-weather models by taking advantage of the dense coverage of wide-swath passive-microwave sensors in low-Earth orbit.

All these encouraging results combined with the technological maturity of small-satellites and miniaturized radars motivate the future development of spaceborne missions to acquire frequent radar observations from a low-Earth orbit. The design study that we conducted assuming a convoy of two spacecraft each with a MiniKaAR radar showed that i) more than 70% of the convection above 5 km of altitude would be observed, ii) an inter-spacecraft separation of ~ 90 s

would be a good compromise between the sensitivity to changes in reflectivity of MiniKaAR and the stationarity of the targeted air mass fluxes, and iii) a pointing accuracy of 0.025° in half rms per spacecraft should warrant the accuracy in the retrieved parameters.

7 Acknowledgements

This work was performed at the Jet Propulsion Laboratory, California Institute of Technology, under contract with the National Aeronautics and Space Administration.

A Appendices

A.1 Estimation of the horizontal advection

To illustrate the digital-image-correlation technique (DICT) [21] used to estimate the advection field $\boldsymbol{U}$, we assume that the reflectivity observations are acquired at times $\mathcal{T} = \{t_\ell,\ \ell \in \mathbb{N}\}$ over a regularly meshed volume. In a Cartesian reference system the volume is denoted $\Omega = \{\boldsymbol{M}_{i,j,k} = (i\Delta_X, j\Delta_Y, k\Delta_Z)\}_{i,j,k}$ with $\Delta_X,\ \Delta_Y,\ \Delta_Z$ the step sizes of the mesh.

Given two consecutive radar data sets $Z(\cdot, t_{\ell-1})$ and $Z(\cdot, t_\ell)$, for every point $\boldsymbol{M}_{i,j,k}$, and for every *horizontal displacement vector* $\boldsymbol{u}$ among the possible displacement vectors $\mathcal{U} \subset \mathbb{R}^2$, a "horizontal neighbourhood" $\mathcal{A}$ is considered about the points $\boldsymbol{M}_{i,j,k}$ and $\boldsymbol{M}_{i,j,k} + \boldsymbol{u}$. The neighbourhood $\mathcal{A}$ is chosen as a square, which covers $(2n+1) \times (2n+1)$ pixels, with $n > 0$. The maximum size of the displacement vectors in $\mathcal{U}$ is chosen according to the maximum distance the cloud/precipitation is expected to advect during the time span $t_\ell - t_{\ell-1}$, whereas the extent of the averaging area $\mathcal{A}$ is chosen according to the spatial correlation length of the features of Z.

The cross-covariance between $Z(\boldsymbol{M}_{i,j,k}, t_{\ell-1})$ and $Z(\boldsymbol{M}_{i,j,k} + \boldsymbol{u}, t_\ell)$ is computed as

$$\rho(\boldsymbol{M}_{i,j,k}; \boldsymbol{u}) = \frac{\mathbb{E}_{\mathcal{A}}\left[\widehat{Z}(\boldsymbol{M}_{i,j,k}, t_\ell)\widehat{Z}(\boldsymbol{M}_{i,j,k} + \boldsymbol{u}, t_{\ell-1})\right]}{\sigma_Z(\boldsymbol{M}_{i,j,k}, t_\ell)\sigma_Z(\boldsymbol{M}_{i,j,k} + \boldsymbol{u}, t_{\ell-1})}, \tag{14}$$

where

$$\begin{aligned}
\widehat{Z}(\boldsymbol{M}_{i,j,k}, t_\ell) &= Z(\boldsymbol{M}_{i,j,k}, t_\ell) - \mathbb{E}_{\mathcal{A}}[Z(\boldsymbol{M}_{i,j,k}, t_\ell)], \\
\sigma_Z(\boldsymbol{M}_{i,j,k}, t_\ell) &= \mathbb{E}_{\mathcal{A}}[\widehat{Z}^2(\boldsymbol{M}_{i,j,k}, t_\ell)], \\
\mathbb{E}_{\mathcal{A}}[f(\boldsymbol{M})] &= \frac{1}{(2n+1)^2} \sum_{k_X=-n}^{n} \sum_{k_Y=-n}^{n} f[\boldsymbol{M} + \boldsymbol{e}(k_X, k_Y)],
\end{aligned}$$

for any function f, with $\boldsymbol{e}(k_X, k_Y) \in \mathcal{U}$ an elementary displacement vector (by k_X pixels along the X axis, and k_Y pixels along the Y axis). As a result, we obtain the list of coefficients $\{\rho(\boldsymbol{M}_{i,j,k}; \boldsymbol{u}),\ \boldsymbol{u} \in \mathcal{U}\}$, from which the displacement vector $\boldsymbol{u}_*$ is obtained as

$$\boldsymbol{u}_*(\boldsymbol{M}_{i,j,k}, t_\ell) = \arg\max_{\boldsymbol{u}\in\mathcal{U}} \rho(\boldsymbol{M}; \boldsymbol{u}, t, \delta_t), \tag{15}$$

and the advection as

$$\boldsymbol{U}(\boldsymbol{M}_{i,j,k}, t_\ell) = \frac{1}{t_\ell - t_{\ell-1}} \boldsymbol{u}_*(\boldsymbol{M}_{i,j,k}, t_\ell). \tag{16}$$

To increase the robustness of the determination of the advection vector, we require that the estimate of $\boldsymbol{U}$ be obtained from a clearly defined maximum of ρ. This amounts to requiring that the Hessian of ρ be non-singular, e.g. by constraining its condition number.

The importance of accounting for the advection when dealing with frontal systems is illustrated using NEXRAD observation of the California Blizzard discussed in Section 3.1. Figure 18 displays the vertical averages of Z (left), $d_t Z$ inclusive of the advection estimated by DICT (middle) and $\partial_t Z$ not accounting for the advection (right), for data at 22:11 (top) or for data averaged between 18:14 and 01:00 (bottom). The strong advection of the storm produces large differences in the maps of $\partial_t Z$ (right) and $d_t Z$ (middle) both in the instantaneous data (top) and their long-term averages (bottom). On the one hand, the map of $d_t Z$ shows the sources of moisture in the South-West originating from the atmospheric river. On the other hand, with $\partial_t Z$ the displacement between consecutive radar measurements leads to a progressive cancellation of features in $\partial_t Z$, as indicated by the smaller range of variation of $\partial_t Z$ compared to $d_t Z$.

B Principal-component and canonical-correlation analyses

B.1 Principal-component analysis

To capture the variability of $Q_{\mathrm{AIR}}(h \geq 0)$, $Z_{\mathrm{AVG}}(h \geq 5\ \mathrm{km})$ and $\Delta_t Z_{[\mathrm{dBZ}]}(h \geq 5\ \mathrm{km})$ in a organized way, a principal-component analysis is applied. The covariance matrices $K_{\mathrm{A}},\ K_{\mathrm{D}},\ K_{\mathrm{Q}}$ are computed over the set $\mathcal{C}$ of convective profiles for Z_{AVG}, $\Delta_t Z_{[\mathrm{dBZ}]}$ and Q_{AIR}, respectively. An eigenvalue decomposition of the covariance matrices yields the eigen-systems $\{\lambda_{\mathrm{A},k}, \boldsymbol{\varphi}_{\mathrm{A},k}\}_{k=1,\ldots,N_1}$, $\{\lambda_{\mathrm{D},k}, \boldsymbol{\varphi}_{\mathrm{D},k}\}_{k=1,\ldots,N_1}$ and $\{\lambda_{\mathrm{Q},k}, \boldsymbol{\varphi}_{\mathrm{Q},k}\}_{k=1,\ldots,N_0}$, with N_0 the number of bins in the entire vertical profile, and N_1 the number of bins above $5\ \mathrm{km}$. The eigenvalues are sorted in decreasing order, i.e. $\lambda_{\mathrm{A},1} \geq \lambda_{\mathrm{A},2} \geq \ldots \geq \lambda_{\mathrm{A},N_1} \geq 0$ and similarly for $\{\lambda_{\mathrm{D},k}\}_{k=1,\ldots,N_1}$ and $\{\lambda_{\mathrm{Q},k}\}_{k=1,\ldots,N_0}$. The principal vectors $\{\boldsymbol{\varphi}_{\mathrm{A},k}\}_{k=1,\ldots,N_1}$, $\{\boldsymbol{\varphi}_{\mathrm{D},k}\}_{k=1,\ldots,N_1}$ and $\{\boldsymbol{\varphi}_{\mathrm{Q},k}\}_{k=1,\ldots,N_0}$ each form orthonormal

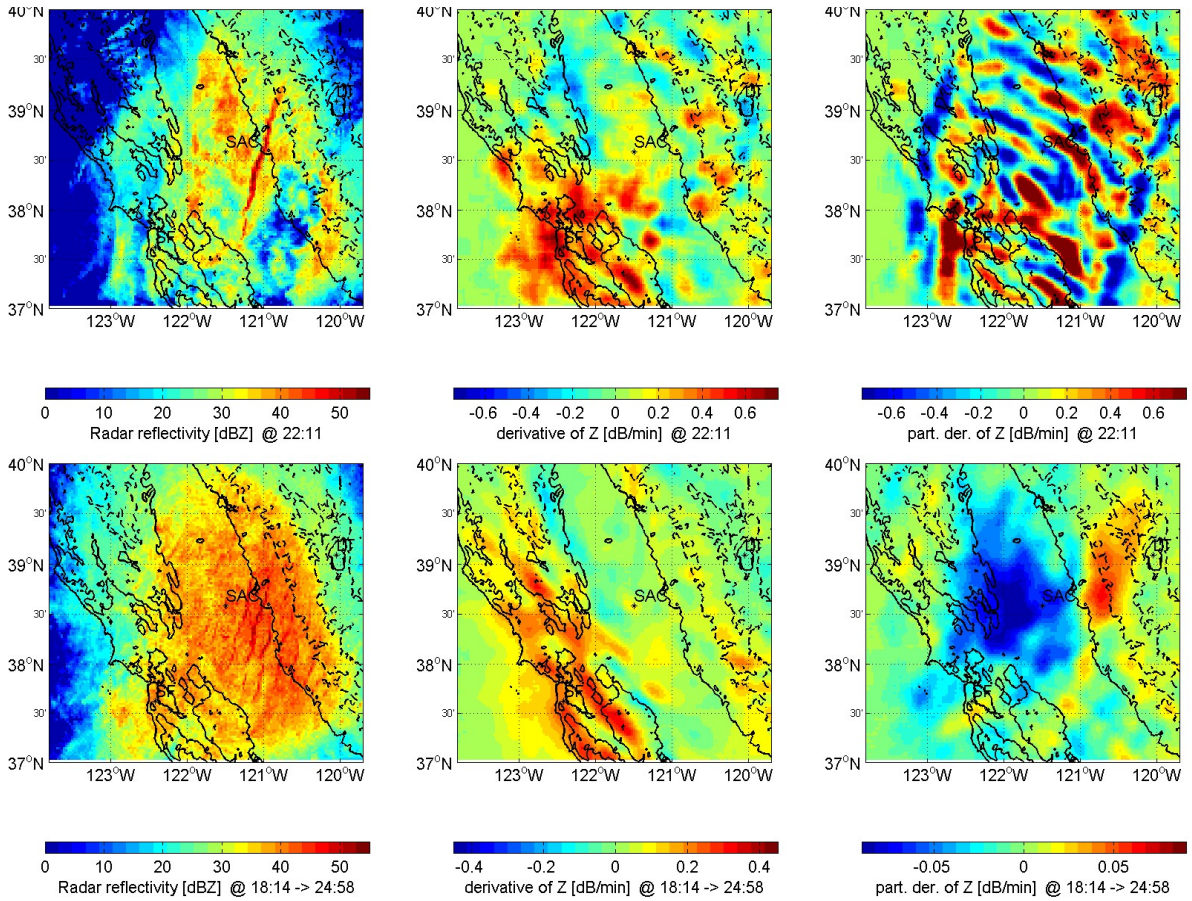

Figure 18: Maps of vertically averaged reflectivity (Z, left panels), associated total derivative ("$d_t Z$" $= \partial Z/\partial t + V \cdot \nabla Z$, center panels) and time derivative ("$\partial_t Z$" $= \partial Z/\partial t$, right panels): the top row shows the instantaneous values at 14:11 PST (during the squall), and the bottom shows the temporal averages from 10:14 to 17:00 PST.

bases onto which the initial fields are projected as follows

$$Q_{\mathrm{AIR}}(\boldsymbol{r},h,t) \approx \sum_{k=1}^{N_0} \eta_{\mathrm{Q},k}(\boldsymbol{r},t)\boldsymbol{\varphi}_{\mathrm{Q},k}(h), \qquad \forall h \geq 0 \text{ km}, \tag{17a}$$

$$Z_{\mathrm{AVG}}(\boldsymbol{r},h,t) \approx \sum_{k=1}^{N_1} \eta_{\mathrm{A},k}(\boldsymbol{r},t)\boldsymbol{\varphi}_{\mathrm{A},k}(h), \qquad \forall h \geq 5 \text{ km}, \tag{17b}$$

$$\Delta_t Z_{[\mathrm{dBZ}]}(\boldsymbol{r},h,t) \approx \sum_{k=1}^{N_1} \eta_{\mathrm{D},k}(\boldsymbol{r},t)\boldsymbol{\varphi}_{\mathrm{D},k}(h), \qquad \forall h \geq 5 \text{ km}, \tag{17c}$$

with

$$\eta_{\mathrm{Q},k}(\boldsymbol{r},t) = \int_0^\infty Q_{\mathrm{AIR}}(\boldsymbol{r},h,t)\boldsymbol{\varphi}_{\mathrm{Q},k}(h)dh, \tag{18a}$$

$$\eta_{\mathrm{A},k}(\boldsymbol{r},t) = \int_5^\infty Z_{\mathrm{AVG}}(\boldsymbol{r},h,t)\boldsymbol{\varphi}_{\mathrm{A},k}(h)dh, \tag{18b}$$

$$\eta_{\mathrm{D},k}(\boldsymbol{r},t) = \int_5^\infty \Delta_t Z_{[\mathrm{dBZ}]}(\boldsymbol{r},h,t)\boldsymbol{\varphi}_{\mathrm{D},k}(h)dh. \tag{18c}$$

The principal components $\{\eta_{\mathrm{A},k}\}_{k=1,\ldots,N_1}$, $\{\eta_{\mathrm{D},k}\}_{k=1,\ldots,N_1}$, $\{\eta_{\mathrm{Q},k}\}_{k=1,\ldots,N_0}$ have vanishing means and variances equal to the eigenvalues $\{\lambda_{\mathrm{A},k}\}_k$, $\{\eta_{\mathrm{D},k}\}_k$ and $\{\eta_{\mathrm{Q},k}\}_k$, respectively. The generally rapid decay of eigenvalues allows to approximate the initial fields using a few terms. For instance, if our objective is to capture at least 80% of the variability of the fields, based on Table 1, Eqs (18) can be truncated to $M_0 = 3$, $M_1 = 2$ and $M_2 = 8$, respectively.

B.2 Canonical-correlation analyses

To find the dominant correlations between the the radar-derived and environmental parameters, a canonical-correlation analysis (CCA) is applied [12]. Using the PCA decomposition, the CCA identifies the linear combinations between components of the observation vector $\boldsymbol{X} = (\eta_{\mathrm{A},1},\ldots,\eta_{\mathrm{A},M_1},\eta_{\mathrm{D},1},\ldots,\eta_{\mathrm{D},M_2})$ that are the most correlated with linear combinations of components of the environmental vector $\boldsymbol{Y} = (\eta_{\mathrm{Q},1},\ldots,\eta_{\mathrm{Q},M_0})$.

The CCA algorithm provides two matrices $A = (a_{i,j}) \in \mathbb{R}^{(M_1+M_2)\times M_{0,1}}$, $B = (b_{i,j}) \in \mathbb{R}^{M_0\times M_{0,1}}$ where $M_{0,1} = \min(M_0, M_1 + M_2)$, and a vector of positive numbers $R_{\mathrm{CCA}} = (r_{\mathrm{CCA}}(1),\ldots,...r_{\mathrm{CCA}}(M_{0,1}))$ with $r_{\mathrm{CCA}}(1) \leq \ldots \leq r_{\mathrm{CCA}}(M_{0,1})$. The matrix A is the matrix of eigenvectors of the matrix $K_{XX}^{-1/2}K_{XY}K_{YY}^{-1}K_{YX}K_{XX}^{-1/2}$ and B is the matrix of eigenvectors of the matrix $K_{YY}^{-1/2}K_{YX}K_{XX}^{-1}K_{XY}K_{YY}^{-1/2}$, where K_{XX} and K_{YY} are the covariance matrices of $\boldsymbol{X}$ and $\boldsymbol{Y}$, while $K_{XY} = K_{YX}^t$ is the cross-covariance between $\boldsymbol{X}$ and $\boldsymbol{Y}$.

As a result, i) the components of $\left\{ u_j = \sum_{i=1}^{M_1+M_2} a_{i,j} X_i \right\}_{j=1,M_{0,1}}$ are mutually statistically uncorrelated, and similarly for $\left\{ v_j = \sum_{i=1}^{M_0} b_{i,j} Y_i \right\}_{j=1,M_{0,1}}$; and ii) for every component $j = 1, \ldots, M_{0,1}$, the statistical correlation between between u_j and v_j equals $r_{\mathrm{CCA}}(j)$.

It is convenient to combine the results of the CCA and PCA by defining the projectors,

$$\boldsymbol{\psi}_{\mathrm{A},j}(h) = \sum_{k=1}^{M_1} a_{k,j} \boldsymbol{\varphi}_{\mathrm{A},k}(h), \tag{19a}$$

$$\boldsymbol{\psi}_{\mathrm{D},j}(h) = \sum_{k=1}^{M_1} a_{M_1+k,j} \boldsymbol{\varphi}_{\mathrm{D},k}(h), \tag{19b}$$

$$\boldsymbol{\psi}_{\mathrm{Q},j}(h) = \sum_{k=1}^{M_0} b_{k,j} \boldsymbol{\varphi}_{\mathrm{Q},k}(h). \tag{19c}$$

With these new variables, the CCA variables u_j, v_j are obtained by applying the CCA projectors to the initial fields as follows

$$v_j(\boldsymbol{r}, t) = \int_0^\infty Q_{\mathrm{AIR}}(\boldsymbol{r}, h, t) \boldsymbol{\psi}_{\mathrm{Q},j}(h) dh, \tag{20a}$$

$$\text{and} \qquad u_j(\boldsymbol{r}, t) = u_{\mathrm{A},j}(\boldsymbol{r}, t) + u_{\mathrm{D},j}(\boldsymbol{r}, t), \tag{20b}$$

$$\text{with} \qquad u_{\mathrm{A},j}(\boldsymbol{r}, t) = \int_5^\infty Z_{\mathrm{AVG}}(\boldsymbol{r}, h, t) \boldsymbol{\psi}_{\mathrm{A},j}(h) dh, \tag{20c}$$

$$u_{\mathrm{D},j}(\boldsymbol{r}, t) = \int_5^\infty \Delta_t Z_{[\mathrm{dBZ}]}(\boldsymbol{r}, h, t) \boldsymbol{\psi}_{\mathrm{D},j}(h) dh. \tag{20d}$$

References

[1] L. Alfieri, P. Claps, and F. Laio, “”time-dependent z-r relationships for estimating rainfall fields from radar measurements”,” *Natural Hazards and Earth System Science*, vol. 10, no. 1, pp. 149–158, 2010. [Online]. Available: http://www.nat-hazards-earth-syst-sci.net/10/149/2010/

[2] P. Barber and C. Yeh, “Scattering of electromagnetic waves by arbitrarily shaped dielectric bodies,” *Applied Optics*, vol. 14, pp. 2864–2872, Dec. 1975.

[3] T. D. Crum, and R. L. Alberty, R., “the wsr-88d and the wsr-88d operational support facility,” *Bull. Amer. Meteor. Soc.*, vol. 74, pp. 1669–1687, 1993.

[4] R. J. Doviak, D. S. Zrnić and D. S. Sirmans, "Doppler weather radar," *Proc. IEEE*, vol. 67, no. 11, pp. 1522–1553, Nov. 1979.

[5] R. J. Doviak and D. S. Zrnic, *Doppler radar and weather observations / Richard J. Doviak, Dusan S. Zrnic*, 2nd ed. Academic Press, Orlando, Fla. :, 1993.

[6] B. T. Draine and P. J. Flatau, "User Guide for the Discrete Dipole Approximation Code DDSCAT 7.3," *ArXiv e-prints*, May 2013.

[7] S. R. Guimond, M. A. Bourassa, and P. D. Reasor, "A Latent Heat Retrieval and Its Effects on the Intensity and Structure Change of Hurricane Guillermo (1997). Part I: The Algorithm and Observations," *Journal of Atmospheric Sciences*, vol. 68, pp. 1549–1567, Aug. 2011.

[8] Z. S. Haddad, D. A. Short, S. L. Durden, E. Im, S. Hensley, M. B. Grable and R. A. Black, "A new parametrization of the rain drop size distribution," *IEEE Transactions on Geoscience and Remote Sensing*, vol. 35, pp. 532–539, May 1997.

[9] Z. S. Haddad and D. Rosenfeld, "Optimality of empirical Z-R relations," *Quarterly Journal of the Royal Meteorological Society*, vol. 123, pp. 1283–1293, Jul. 1997.

[10] A. K. Heidinger, C. O'Dell, R. Bennartz, and T. Greenwald, "The Successive-Order-of-Interaction Radiative Transfer Model. Part I: Model Development," *Journal of Applied Meteorology and Climatology*, vol. 45, pp. 1388–1402, Oct. 2006.

[11] S.-Y. Hong and J.-O. J. Lim, "The WRF single-moment 6-class microphysics scheme (WSM6)," *J. Korean Meteor. Soc.*, vol. 42, no. 2, pp. 129–151, 2006.

[12] H. Hotelling, "Relations between two sets of variates", *Biometrika*, vol. 28, pp. 321377, 1936.

[13] R. A. Houze Jr., *Cloud dynamics*, ser. International Geophysics (Book 53). Academic Press, 1994.

[14] E. Kalnay, *Atmospheric Modeling, Data Assimilation and Predictability*. Cambridge University Press, Dec. 2002.

[15] L. Liao and K. Sassen, "Investigation of relationships between Ka-band radar reflectivity and ice and liquid water contents," *Atmospheric Research*, vol. 34, pp. 231–248, 1994.

[16] Y.-L. Lin, R. D. Farley, and H. D. Orville, "Bulk Parameterization of the Snow Field in a Cloud Model." *Journal of Applied Meteorology*, vol. 22, pp. 1065–1092, Jun. 1983.

[17] E. Peral, S. Tanelli, Z. Haddad, O. Sy, G. Stephens, and E. Im, "Raincube: A proposed constellation of precipitation profiling radars in cubesat," in *Geoscience and Remote Sensing Symposium (IGARSS), 2015 IEEE International*, July 2015, pp. 1261–1264.

[18] V. Petković and C. D. Kummerow, "A Spatiotemporal Correlation Technique to Improve Satellite Rainfall Accumulation," *Journal of Applied Meteorology and Climatology*, vol. 51, pp. 2122–2136, Dec. 2012.

[19] F. M. Ralph, P. J. Neiman, G. N. Kaladis, and K. Weickman, "A multiscale observational case study of a Pacific atmospheric river exhibiting tropical-extratropical connections and a mesoscale frontal wave," *Monthly Weather Review*, vol. 139, pp. 1169–1189, Apr. 2011.

[20] F. M. Ralph, T. Coleman, P. J. Neiman, R. J. Zamora, and M. D. Dettinger, "Observed impacts of duration and seasonality of atmospheric-river landfalls on soil moisture and runoff in coastal northern California," *Journal of Hydrometeorology*, vol. 14, pp. 443–459, Apr. 2013.

[21] C. Su and L. Anand, "A New Digital Image Correlation Algorithm for Whole-field Displacement Measurement," *Innovation in Manufacturing Systems and Technology (IMST)*, 2003. [Online]. Available: http://hdl.handle.net/1721.1/3749

[22] G. Thompson, P. R. Field, R. M. Rasmussen, and W. D. Hall, "Explicit Forecasts of Winter Precipitation Using an Improved Bulk Microphysics Scheme. Part II: Implementation of a New Snow Parameterization," *Monthly Weather Review*, vol. 136, p. 5095, 2008.

[23] P. C. Waterman, "Symmetry, Unitarity, and Geometry in Electromagnetic Scattering," *Phys. Rev. D.*, vol. 3, pp. 825–839, February 1971.

[24] A. J. Wimmers and C. S. Velden, "MIMIC: A New Approach to Visualizing Satellite Microwave Imagery of Tropical Cyclones," *Bulletin of the American Meteorological Society*, vol. 88, p. 1187, 2007.